hiPSC-derived 3D Bioprinted Skeletal Muscle Tissue Implants Regenerate Skeletal Muscle Following Volumetric Muscle Loss

Yasamin A. Jodat
Brigham and Women's Hospital, Harvard Medical School
Ting Zhang
Tsinghua University
Ziad Al Tanoury
Brigham and Women's Hospital, Harvard Medical School
Tom Kamperman
University of Twente https://orcid.org/0000-0002-2835-6709
Kun Shi
Brigham and Women's Hospital, Harvard Medical School
Yike Huang
Brigham and Women's Hospital
Adriana Panayi
Brigham and Women's Hospital
Yori Endo
Brigham and Women's Hospital
Xichi Wang
Brigham and Women's Hospital, Harvard Medical School
Jacob Quint
University of Nebraska–Lincoln
Adnan Arnaout
Brigham and Women's Hospital, Harvard Medical School
Kiavash Kiaee
Brigham and Women's Hospital, Harvard Medical School
Shabir Hassan
Brigham and Women's Hospital, Harvard Medical School
Junmin Lee
UCLA https://orcid.org/0000-0002-4414-7130
Angel Flores Huidobro Martinez
Brigham and Women's Hospital, Harvard Medical School
Sofia Lara Ochoa

Brigham and Women's Hospital, Harvard Medical School

KangJu Lee

University of California Los Angeles

Michelle Calabrese

Chemical Engineering and Materials Science Department

Alessandro Carlucci

Brigham and Women's Hospital, Harvard Medical School https://orcid.org/0000-0001-7590-5283

Ali Tamayol

University of Nebraska

Indranil Sinha

Brigham and Women's Hospital

Olivier Pourquié

Harvard Medical School https://orcid.org/0000-0001-5189-1227

Su Ryon Shin (shin.lotus@gmail.com)

Brigham and Women's Hospital, Harvard Medical School

Article

Keywords: Skeletal muscle engineering, induced pluripotent stem cells, bioprinting, engineering vascularized tissues, volumetric muscle loss

Posted Date: January 20th, 2021

DOI: https://doi.org/10.21203/rs.3.rs-146091/v1

Abstract

Engineering of biomimetic tissue implants provides an opportunity for repairing volumetric muscle loss (VML), beyond a tissue's innate repair capacity. Here, we present thick, suturable, and pre-vascularized 3D muscle implants containing human induced pluripotent stem cell-derived myogenic precursor cells (hiPSC-MPCs), which can differentiate into skeletal muscle cells while maintaining a self-renewing pool. The formation of contractile myotubes and millimeter-long fibers from hiPSC-MPCs is achieved in chemically, mechanically, and structurally tailored extracellular matrix-based hydrogels, which can serve as scaffolds to ultimately organize the linear fusion of myoblasts. Embedded multi-material bioprinting is used to deposit complex patterns of perfusable vasculatures and aligned hiPSC-MPC channels within an endomysium-like supporting gel to recapitulate muscle architectural integrity in a facile yet highly rapid manner. Moreover, we demonstrate successful graft-host integration and de novo muscle formation upon in vivo implantation of pre-vascularized constructs within a VML model. This work pioneers the engineering of large pre-vascularized hiPSC-derived muscle tissues toward next generation VML regenerative therapies.

Introduction

Volumetric muscle loss (VML), often caused by traumatic events, involves the *en bloc* loss of skeletal muscle and results in poor muscle function. These injuries often overwhelm the intrinsic ability for muscle to repair itself and instead lead to extensive fibrosis.[1,2] Functional muscle transfer, which involves the transplantation of vascularized muscle from a donor, is a standard approach for VML treatment.[3] However, shortages of donor tissue, donor-site morbidity, and suboptimal reconstitution of muscle defects impair functional recovery.[3-5] Myogenic implants obviate some of these concerns, but also fail to fully reconstitute muscle function following VML injury. Impaired muscle regenerative capacity in implant flaps has been linked to the lack of engraftable muscle stem (i.e., satellite) cells and the limited functional differentiation of these cells into *de novo* myofibers.[6] As such, developing clinically relevant, functional tissue implants using autologous cells, which are capable of muscle regeneration, has emerged as a potential solution.

Bioengineering clinically relevant muscle tissue implants with the capacity for muscle regeneration requires identifying and embedding skeletal muscle stem cells, as well as controlling the cellular alignment and differentiation within the engineered 3D scaffolds to reconstitute the architecture of skeletal muscle. 3D bioprinted skeletal muscle constructs have shown increased myofiber differentiation and promising *in vivo* results.[7] However, the majority of these constructs rely on primary myogenic (progenitor) cells that possess limited proliferation capacity and lose their myogenic potential during serial *in vitro* passaging,[8] thereby hampering the clinical translation of VML therapies. In contrast, human induced pluripotent stem cells (hiPSCs) exhibit excellent proliferation potential,[9,10] and are capable of being differentiated into myogenic (progenitor) cells and regenerating skeletal muscle, similar to satellite cells.[11,12]

The striking ability of hiPSC-derived muscle precursor cells (MPCs) to self-organize by forming primary and secondary muscle fibers in a 2D *in vitro* culture system is similar to the muscle organization process observed *in vivo*.[13] To implement this ability of hiPSC-MPCs in 3D implants, a biomaterial must provide adequate stem cell niches that guide myogenic differentiation and maturation by providing the right instructive cues and inducing cell alignment.[14-16] Furthermore, functional vascular networks should be interwoven into the volumetric implants to minimize diffusion limitations and to serve as guides for the ingrowth of host endothelial cells (ECs) and hematopoietic cells, thereby achieving timely angiogenesis and preventing necrosis in the core of thick (> 1 mm) engineered tissues.[17,18] The rapid vascularization of volumetric muscle constructs based on hiPSC-MPCs is of paramount importance for the cells' survival, myogenic differentiation, and maturation into functional myofibers, as these cells are metabolically active.[19-22]

A common approach for building 3D implants has been the mold fabrication of hydrogel encapsulated isogenic 3D hiPSC-derived artificial skeletal muscle constructs, which gives limited control over architecture.[23] Here, we propose a strategy of combining 3D bioprinting and hiPSC-MPC culture technologies to engineer pre-vascularized muscle tissue implants that emulate the intricate structural complexity and multi-dimensional hierarchy of native muscle, thus forming the basis for a new generation of VML repair strategies (**Figure 1**). An embedded multi-material bioprinting (EMB) paradigm was selected, enabling the rapid and high-resolution bioprinting of aligned muscle fibers and vascular free-forms within a liquid support matrix which could be solidified on demand.[24-26] A low viscosity and thermally reversible gelatin-methacryloyl (GelMA)-based bioink was used, as it would mitigate the lethal shear stresses on cells that typically induce cell membrane damage or even cell death during the rapid extrusion of bioinks through nozzles.[27-31] To create perfusable channels, a sacrificial gelatin bioink was printed between the engineered muscle fibers and then seeded with human umbilical vein endothelial cells (HUVECs). To study the levels of anastomosis and graft-host integration on a cellular level, the pre-vascularized constructs were subcutaneously implanted in a murine model. Furthermore, a nanofibrous suturable scaffold was integrated onto the printed construct to achieve a prolonged retention of the implants in the injury site. Finally, we established an *in vivo* VML repair proof-of-concept by implanting the hiPSC-MPC engineered muscle fiber bundles within a VML-injured mouse model. We thereby introduce a bioprinting strategy to efficiently engineer clinically relevant skeletal muscle tissues comprising millimeter-long striated and contractile muscle fibers from differentiated and matured hiPSC-MPCs.

Results And Discussion

EMB for fabricating muscle fiber bundle architectures

The EMB strategy consists of directly printing a hiPSC-MCPs-laden bioink within a pre-gelled GelMA supporting matrix, unlike conventional embedded printing methods in which inks are typically printed within microgels and slurries (**Figure 1**).[27,28] To form millimeter-long myofibers, hiPSC-MPCs must be

anchored via abundant Arginyl-glycyl-aspartic acid (RGD) binding sites on the engineered ECM matrix, which ultimately organize the linear fusion of myoblasts, similar to the native ECM.[32,33] The bioink for muscle fibers consists of gelatin and GelMA, both of which contain denatured collagen, a major ECM component of skeletal muscle tissue with abundant RGD binding sites. By adjusting the concentration of GelMA and the crosslinking density, we can easily tune the porosity and degradation of the hydrogels[34] in order to achieve adequate mechanical support and degradation behaviors for the engineering of myofibers with hiPSC-MPCs. The role of the GelMA supporting matrix is comparable to the hierarchical ECM structure of the native endomysium, which is mainly composed of type I and type III collagens.[35] This surrounding connective tissue physically supports densely bound aligned myofiber bundles and perfusable vessels,[36] preventing structural collapse during muscle contractions and movements. In addition, the incorporation of GelMA pre-polymers in both the supporting matrix and the bioink prevents the delamination of the bioprinted layers upon photo-crosslinking.

The thermally reversible gelation properties of both gelatin and GelMA enable a straightforward temperature-controlled printing process.[37,38] Complex multi-layered patterns can be fabricated by harnessing the reversible thermal-healing properties of the GelMA supporting matrix just below the gelation temperature (between ~8 °C and ~20 °C, sol-gel state) (**Figure 2 and S1**). To achieve an integrated crack-free embedded structure, *ad hoc* heating of the bioink-containing nozzle (up to 37 °C) can be used to partially melt the interfacing areas of the sol-gel supporting matrix (**Figure S2**). This thermal-healing behavior was corroborated by visibly reduced shape fidelity and the formation of micro-sized cracks when printing at a lower support matrix temperature (~6 °C). To maintain shape fidelity, the bioink stiffness could be increased through increasing polymer concentration (**Figure 2b, c**). However, higher mechanical stiffness is a tradeoff that reduces biocompatibility with soft tissues and laden cells. Alternatively, gelatin can be added to the GelMA bioink to temporarily increase its stiffness and viscosity for bioprinting followed by a post-crosslinking removal step at ~37 ^{o}C,[39] creating non-merged parallel channels (**Figure 2d**). By adjusting ink flow rates and nozzle translational speed, the diameter of the bioprinted channels could be tuned (160±8 to 220±16 μm) (**Figure S3**). Changing the center-to-center inter-channel distance did not significantly affect the shape fidelity and the distance could be reduced to the length of almost one channel diameter before the channels started to merge (**Figure S4**). This distance is comparable to the diffusion limit of the native skeletal muscle environment and thus helps with the engineering of large viable tissues.[40] To obtain aligned channels resembling muscle architecture, we printed vertically aligned microfibers within the supporting matrix with this minimal spacing, thus increasing the density of the muscle tissue. We set out to use a photo-crosslinking strategy to transform the embedding bath, including the printed patterns, into a solid hydrogel scaffold that was robust enough to enable *in vitro* culture, *in vivo* implantation, and ultimately, muscle tissue repair (**Figure 2e,f**). To this end, various concentrations of GelMA and photo-crosslinking conditions (i.e., UV exposure time) were assessed to obtain a solid construct with mechanical properties optimized for muscle stem cell differentiation and maturation. This screening was also based on our previous studies that focused on identifying the necessary mechanical properties for a hydrogel to mimic the native skeletal tissue ECM (i.e., 10-50 kPa and >30% elastic strain).[41] Using a 5% (w/v) GelMA matrix, we investigated stiffness as a

function of UV exposure duration (**Figure 2g** and **S5a**). The optimum UV condition (55 s, 5.5 J/cm^2), with a matrix stiffness of ~8 kPa after 21 days of *in vitro* culture (**Figure S5b**), resulted in a stable construct that prevented the collapse of the printed patterned geometries during long-term tissue culture.

The EMB of the recurring micropatterns was demonstrated by rapidly printing various longitudinally aligned patterns with high printing density within a relatively large-sized supporting bath (1 cm^3), thus abstractly representing the vessels and muscle fibers in a native muscle fiber bundle (**Figure 2h, i** and **S6**). Longitudinal patterns could also be combined with the printing of transversal patterns (**Figure 2j**). In addition, coaxial bioinks could be easily incorporated into the EMB technique to fabricate patterned arrays of core-shell microfibers in the supporting bath (**Figure 2k**). The thicknesses of the core and sheath could be tuned by adjusting the diameter of the coaxial nozzles (**Figure S7**). Complex 3D shapes such as fractal-like branched networks containing aligned microfibers could also be printed in this supporting gel to recapitulate the architecture of four different types of natural vascularized skeletal muscle flaps (**Figure 2l-o,** < 5 min print time per construct). The proposed EMB technology can facilitate the fabrication of large-sized vascularized tissue implants through modulating the size and geometry of the supporting matrix. Alternatively, centimeter-scale building blocks could be assembled into even larger constructs using 3% (w/v) GelMA as UV-curable glue. Gluing together nine uniquely patterned building blocks readily resulted in the formation of large, complex, and perfusable 3D constructs with volumes of almost 10 cm^3 (**Figure 2p**).

Perfusable construct engineering

To endow engineered tissue constructs with perfusable vascular-like networks, a thermo-reversible gelatin ink was formulated, which could be removed by warming up the photocured GelMA supporting matrix to 37 °C in PBS or cell culture media (**Figure 3a**). The method readily enabled the fabrication of a bifurcating channel network within a ~1 cm^3 supporting matrix (**Figure 3b**) and enabled the controlled screening of bioengineering parameters such as vessel diameter, number, and density. Specifically, printing 5% (w/v) gelatin within a 5% GelMA matrix at 2 mm/s formed open and stable channels (diameter = 336.5±34.9 μm) (**Figure 3c**). Although the fabricated channels were larger than the native blood vessels in skeletal muscle, we anticipated that the addition of such perfusable vessels inside a large implant could accelerate the host's blood invasion post implantation, facilitate the formation of micro-capillaries, and ultimately, promote implant integration. Scanning electron microscopy (SEM) imaging of freeze-dried constructs confirmed printed channel patency (**Figure 3d-f**), which was corroborated by successfully perfusing the channels with fluorophores that also represented the perfusion and diffusion of nutrients, growth factors, and waste products in these constructs (**Figure 3g,h** and **Movie S1**). Time-lapse confocal fluorescence imaging revealed a uniform diffusion gradient of the fluorescent-labeled dextran (~20 kDa) within the supporting matrix, which was characterized by a relatively high diffusional permeability (P_d =

7.25 ± 0.675 x 10^{-5} cm s^{-1}), thus favoring the exchange of cellular nutrients and waste products and corresponding to previously reported values (**Figure 3i,j**).[42,43]

In order to explore the vascularization of the perfusable channels, we incorporated HUVECs into the constructs (**Figure 3k**). In two weeks, the HUVECs proliferated and migrated along the channel wall, thereby forming a tubular cellular network that covered the entire channel's interior throughout the construct (**Figure 3l-n**). The complete endothelialization of the perfusable channels was confirmed by the positive staining of platelet endothelial cell adhesion molecules (PECAM/CD31), a biomarker found in the intercellular junctions of ECs. To facilitate the formation of vascular networks throughout the construct, HUVECs were also embedded in the crosslinkable GelMA supporting matrix. In some areas of these constructs, small CD31-positive sprouts connected to the endothelialized perfusable channels were found (**Figure 3o,p**). It was observed that HUVECs embedded in 5% (w/v) GelMA started to proliferate after three days of *in vitro* culture, while HUVECs within 7% (w/v) GelMA did not (**Figure S8**). Furthermore, we observed that embedding HUEVCs in the supporting bath can promote the diffusion of biomolecules across the thick bath **(Figure S9),** potentially due to the increased porosity. HUVEC-laden baths can therefore compensate for the delayed biomolecule diffusion from the endothelial-seeded perfusable channels into the supporting matrix, an observation previously shown to occur due to the formation of vascular junctions and endothelial barrier layers.[44,45]

hiPSC-based muscle fiber bundle engineering

Next, we set out to explore the optimal bioink conditions for hiPSC-MPCs to mature and differentiate inside perfusable bioprinted constructs. Among the printable gel mixtures inside a 5% GelMA supporting matrix (previously discussed in **Figure 2d**), 7.5% (w/v) GelMA bioink (stiffness = 40±8 kPa, further reduced to 22±2 kPa after 3 weeks of incubation in standard culture medium) provided a 3D microenvironment that was mechanically ideal for the myogenic induction of hiPSC-MPCs (i.e., 10-50 kPa and >30% elastic strain) (**Figure S10**).[41,46] To this end, 3- to 4- week old hiPSC-derived progenitor cells were obtained following our previously described serum-free differentiation protocol **(Figure S11)** [11,47] and were encapsulated in a bulk supporting matrix or bioink for 3D culture studies. Further steps of myogenic induction were carried out by delivering differentiation factors to the hiPSC-MPC-laden constructs. Initially, we encapsulated hiPSC-MPCs in 7.5% (w/v) GelMA **(Figure 4a)** and cultured the constructs for 4 weeks to investigate cellular behaviors modulated by UV crosslinking and cell density (**Figure S12).**[48-50] hiPSC-MPCs exhibited increased cell spreading and elongation with shorter UV exposure times and higher cell concentrations. The 7.5% (w/v) GelMA hydrogels were most compatible with the long-term 3D culture of hiPSC-MPCs and the development of striated myofibers with well-organized sarcomeres, while also containing a pool of satellite cells, indicated by positive Actn2, Pax7, MyoG, Titin, and MyHC staining (**Figure 4b-e** and **S13**). Additionally, spontaneous contractile activity was

observed in encapsulated hiPSC-MPCs in 7.5% (w/v) GelMA after 15 days of *in vitro* culture (**Figure 4f** and **Movie S2**).

The optimized muscle bioink was used in conjunction with the optimized EMB to obtain vertically aligned hiPSC-MPC-laden microfibers at a density of ~7 fibers/mm^2. **(Figure 4g)**. Specifically, a pattern of straight fibers (diameter = 184.4±22.3 μm) containing hiPSC-MPCs (20×10^6 cell/mL) in gelatin/GelMA bioink was printed. The differentiated cells remained viable for at least four weeks of *in vitro* culture (**Figure 4h** and **S14**). We successfully fabricated striated, millimeter-long muscle fibers within the printed microfibers using hiPSC-MPCs **(Figure 4i)**. These results highlight the capacity of hiPSC-laden printed fibers to create mesoscale functional muscle tissue. However, when printing the optimized hiPSC-laden bioink within larger constructs (i.e., 5 x 5 x 5 mm^3) without perfusion channels, the cells expressed notably less satellite and mature muscle differentiation markers (Pax7, MyoG, and MyHC) after three weeks, as compared to the same cells cultured in smaller hydrogel constructs (**Figure 4j** vs **Figure 4b,c**). It was hypothesized that the large non-perfused printed constructs (i.e., 5 x 5 x 5 mm^3) hampered the diffusion of nutrients and waste products to sustain hiPSC-MPC maturation and differentiation. Indeed, comparing the viability and metabolic activity of C2C12 myoblast cells in perfusable vs non-perfusable GelMA constructs corroborated this hypothesis (**Figure S15**).

Perfusable channels were printed at various distances and in parallel with the hiPSC-MPC-laden fibers (**Figure S16**) to define the maximum perfusion distance for maintaining high cell viability (~450 μm). A ~1:4 channel-to-fiber ratio rescued the engineered myogenic phenotype, as confirmed by increased biomarker expression (**Figure 4k** and **S17**). hiPSC-MPCs in both perfused and non-perfused constructs demonstrated high cell growth, alignment, and spatial confinement (**Figure 4j**,**k** (F-actin row)). A fast Fourier transform (FFT) was performed to assess the degree of myofiber alignment in both conditions. Interestingly, the alignment index of hiPSC-MPCs printed in constructs with and without perfusable channels after 10 days *in vitro* was not significantly different (**Figure 4l**). However, we observed differences in the clustered alignment of myofibers between the two groups **(Figure S18)**. In non-perfused constructs, three angle peaks were observed (-45º, 0º, and 50º), indicating relatively scattered myofiber alignment along the printed patterns. In contrast, a single peak at approximately 0º was observed in perfused constructs, as well as an average alignment index of 1.5, indicating improved myofiber alignment and fusion along the printed pattern. This data supports the formation of a stronger myofiber fusion along a single axis, which confirms improved muscle fiber maturation in perfused patterned constructs.

The renewal of satellite cells and the differentiation to newly formed myofibers follows three stages, beginning with high Pax7 but negligible MyoD expression in the quiescent satellite cells.[51] Upon muscle injury, the transient inflammatory response, and specifically the recruitment of M2 macrophages, induces the activation and proliferation of satellite cells, marked by an increased expression of MyoD and continued Pax7 expression. Finally, as satellite cells differentiate into myoblasts and fuse to form new myofibers, Pax7 expression declines followed by an increased expression of mature muscle markers

including MyoG (a characteristic indication of intermediate myogenic muscle maturation) and MyHC. In our non-perfused *in vitro* engineered muscle constructs, we observed reduced Pax7 expression from day 10 to 20 (**Figure 4m**), arrested or delayed myogenic differentiation marked by moderate MyoG (**Figure 4n**), and reduced MyHC expression compared to the perfused constructs (**Figure 4o**). This could be attributed to the ischemic necrosis caused by inefficient transfer of nutrients and oxygen in these constructs. The expression dynamics in perfused engineered constructs confirmed this hypothesis, as Pax7 expression sharply increased between days 10 and 20 (**Figure 4m**), indicating high levels of satellite cell activation and proliferation. Moreover, the efficient vascularization and nutrient transfer in the perfused constructs led to increased MyHC expression (**Figure S19**) and a ~5-10 fold higher fusion index (**Figure 4o**), indicating accelerated myogenic differentiation and the formation of MyoG-low, MyHC-high mature myofibers (**Figure 4n**). Muscle cell maturation in the bioprinted constructs was further confirmed on day 20 with ~60% MyHC positive cells (**Figure 4o**) and Actin2-positive fibers with a characteristic sarcomeric pattern (**Figure 4p,q** and **Figure S20**), while the expression of an earlier marker, MyoG, was decreased to ~20%. Detailed SEM analysis of acellular printed muscle bioink revealed an aligned and nanofibrous structure, which might have contributed to the successful confinement, alignment, and maturation of hiPSC-MPCs (**Figure 4r**).[52] Interestingly, the pore size of the engineered endomysium (i.e., supporting matrix) was much bigger than that of the muscle bioink. Together, these results indicate that the incorporation of perfusable channels can facilitate the diffusion of nutrients and waste products, thereby enabling the engineering of relatively large functional tissues that are required for VML repair. Furthermore, the abundant presence of Pax7-positive muscle stem cells, which provide long-term regenerative capacity, is an important feat, one which is also present in newly regenerated skeletal muscle tissue.[53]

To predict and potentially prevent the damaging of *in vivo* implanted constructs, which undergo incessant physical stress and friction at the implant-host tissue interface during body movements, we studied the mechanical properties of the printed constructs. The constructs that contained printed fibers and channels remained intact during 30 days of *in vitro* culture, and the stiffness and elongation at break were not significantly different than those of the bulk supporting matrix without printed channels and fibers (i.e., non-printed construct) (**Figure S21**). Furthermore, the printed constructs showed persistent elastic behavior during cyclic mechanical loading up to 40% strain and did not demonstrate any fatigue (**Figure 4t**), a behavior similar to native skeletal muscle that tolerates cyclic contraction-relaxation stress with excellent elasticity during muscle activity.[54,55] These results indicate that the mechanical properties of the printed constructs could aid in preventing the collapse of perfusable vessels and could physically support the aligned myofibers against cyclic stresses during the regeneration process after *in vivo* implantation.

Pre-vascularized grafts facilitate in vivo cell survival and successfully integrate with host

We explored the subcutaneous *in vivo* grafting of the vascularized printed constructs with different designs (**Figure 5**). The first implant design **(Figure 5a)** contained a bifurcating network coated with HUVECs (~1 cm^3), and exhibited angiogenesis stimulation after 3 weeks along with a substantial number of *de novo* lumens (white arrows) throughout the thick construct (**Figure 5b**). HUVEC-laden bulk GelMA constructs (i.e., non-printed) of the same size (**Figure 5c**) showed fewer vascular lumens in the areas where the hydrogel interfaced with the native tissue (**Figure 5d**). These findings suggest that the formation of micro-vessels in our hydrogels was triggered by the implanted cells, and not only through the host's blood invasion. This finding was previously observed in organized human EC constructs patterned into cords via microfabrication which acted as templates for guided vascularization upon implantation *in vivo*.[56]

Next, to quantitatively investigate the impact of 3D patterned perfusion and pre-endothelialization on both printed constructs and host cell infiltration, four groups (G1-4) were prepared: 3D bioprinted perfusable channels seeded with HUVECs were printed within a supporting matrix of acellular (G1) (**Figure 5e,f**) or HUVEC-laden (G2) (**Figure 5g,h)** constructs. As control groups, 3D bioprinted non-endothelialized perfusable channels in supporting matrix constructs (G3), and non-printed bulk HUVEC-laden supporting matrix (G4) constructs were prepared (**Figure S22**)**.** After one week of *in vivo* culture, the perfusable channels (G1-3) were infiltrated by red blood cells and showed clear signs of endothelialization (**Figure 5e-h and Figure S23**). In these constructs, relatively fast infiltration and a high accumulation of murine vascular networks near the graft-host interface were observed. Together with the observation that the scaffolds completely integrated with the host tissue (**Figure S23**), this data confirmed that the engineered muscle constructs were biocompatible. Both murine CD31-positive cells (i.e., from the host) and human CD31-positive cells (i.e., from the implanted HUVECs) were observed inside the perfusable constructs (**Figure 5f(i), h(i)**). Moreover, embedding HUVECs in the engineered endomysium-like matrix promoted sprouting near the edges of the printed channels (**Figure 5h**). At the surrounding tissue site, the migration and outgrowth of transplanted HUVECs was found (**Figure 5f (iii)**). In the control groups (**Figure S22 a(iii) and b(iii)),** murine ECs were mostly found in the surrounding tissues. In G2 specifically, several vessels consisting of concentrically patterned murine and human endothelial cells were observed (**Figure 5h (iii)**), corroborating with the excellent graft-host integration.

At the three-week harvest timepoint, the perfusable constructs were overgrown by vasculature, including within the channels, indicating anastomosis with the host (**Figure 5f (ii)** and **S22**). Human and murine-positive CD31 cells inside G1 and G2 demonstrated full infiltration of the murine vascular network into the proliferative HUVEC networks (**Figure 5f (ii) and 5h (ii)**). In the tissue surrounding G2, a prevalent presence of migrated HUVECs from the pre-vascularized channels to the host-tissue interface was observed in comparison with G1, possibly due to larger HUVEC density and the formation of sprouting networks at a higher rate (**Figure 5f (iv) and 5h (iv)**). G3 and G4 constructs did not show such clear graft-host integration (**Figure S22**).

G2 exhibited the highest degradation rate and the smallest remaining hydrogel area after harvest (**Figure 5i**). Presumably due to their perfusable geometry, G2 constructs allowed for accelerated biomaterial

degradation through the accumulation of host cytokines including TNF-α, which would trigger foreign body response and an increased expression of metalloproteinase1/3 (MMP1/3), leading to gelatin degradation.[57] We compared the level of construct grafting temporally and spatially by quantifying human and murine CD31-positive vessels within G1 and G2 perfusable channels and the surrounding tissue (**Figure 5j,k**). Although initially (week 1) lower, the number of murine vessels in the channels were increased after 3 weeks to match the number of human vessels (**Figure 5j**), which in turn increased by ~5-10 fold over time. The total number of vessels inside the perfusable channels increased by ~2.5 fold over 3 weeks (**Figure 5k**), indicating a gradual formation of vascular networks between the implanted and host's ECs, similar to previous studies.[58-60] The gradual decline in the number of vessels inside the tissue surrounding G2 was pertained to the pre-existence of ECs and vascular networks embedded inside the supporting matrix, which had induced a much higher number of vessels in the hydrogel-host interface than the channels at the initial stages of infiltration. Moreover, the presence of perfusable channels significantly increased the survival of cells in the transplanted constructs (**Figure 5l**). Overall, the perfusable bioprinted constructs exhibited excellent biocompatibility and interaction with the host vasculature, and pre-endothelized channels and supporting matrices showed significant impact on host infiltration, and implant integration.

Pre-vascularized hiPSC-MPC laden constructs enhance engraftment in volumetric muscle injury model

Finally, we aimed to prove the concept of repairing VML in the quadriceps femoris muscle of a rat. To prevent the sample dislocation and to facilitate integration with the host, we integrated the implants with suturable nanofibrous scaffolds made of a mixture of polyglycerol sebacate and polycaprolactone (PGS/PCL) (**Figure 6a**). Previously, we demonstrated the biocompatibility and biodegradability of these electrospun scaffolds for *in vivo* wound repair and stimuli-responsive drug delivery.[61] Here, we used a photo-crosslinkable glue composed of 5% (w/v) GelMA pre-polymer solution to attach the 3D bioprinted constructs to the scaffolds using UV irradiation (**Figure 6b**). Successful adhesion was revealed by SEM imaging of the hydrogel-nanofibrous scaffold interface (**Figure 6c,d**). The mechanical characterization of the sutured nanofibrous electrospun scaffolds revealed an elastic modulus of 16.4±5.8 MPa and an ultimate tensile strength (UTS) of 1.5±0.7 MPa, which were comparable to reported values (**Figure 6e-g**).[62] Stretching the composite scaffold did not result in fracture at the suture point, suggesting that the suture could tolerate high mechanical stress and large dynamic movement post-surgery.

To create a VML injury model, a rectangular incision was made into a mouse's quadriceps femoris, as previously reported.[63] Approximately 2x3x6 mm^3 of murine muscle volume (corresponding to 0.19 ± 0.005 % of the mouse's total weight) was removed to represent VML injury models.[64-66] 3D vascularized muscle tissue constructs (i.e., V3) glued to PGS/PCL membranes were placed into the muscle wound with

the membrane facing up (**Figure 6h**). Additional groups of acellular GelMA constructs with perfusable channels (i.e., V2) and VML incision with no treatment (i.e., V1) were studied. A layer of fibrotic capsule was observed around the V3 implant four weeks post implantation (**Figure 6i**, V3) with proliferation, and later with the migration of host cells into the construct. At the graft-host interface, newly regenerated muscle tissue was identified (**Figure 6j**) by the presence of centered (as opposed to marginal) nuclei with smaller nucleus diameters across several myofibers.[67,68] Moreover, a strong expression of embryonic skeletal muscle myosin heavy chain (MYH3) was found near V3 scaffolds (**Figure 6i**, MYH3/DAPI) and in myofibers with centered nuclei in both cross-sectional and longitudinal muscle tissues **(Figure 6k)**, suggesting that the incorporation of vascularized hiPSC-MPC laden scaffolds would increase *de novo* muscle regeneration. V2 scaffolds were significantly less incorporated and showed lower *de novo* muscle formation during the same four-week period (**Figure 6i**, V2). High proliferation and some MYH3 expression were notable at the graft-host interface, which was higher than the V1 scaffolds that underwent minimal change after six weeks (**Figure 6i**, V1). The grafting of the implanted hiPSC-derived muscle cells and the stemness of the satellite cells were confirmed by the presence of Pax-positive in the V3 constructs (**Figure 6l**) at a relatively higher level than V2 and V1 (**Figure S24a, b(i-ii)**) and with numerous Pax-positive nuclei on the edges between the myofibers. Although Pax expression, thus regeneration capacity, was found to be higher in the hydrogel implants (V2-3) than the untreated group (V1), it is unclear whether the Pax-positive cells are of human origin. Further characterization with human specific markers can help to isolate the regenerative effect of hiPSCs from native muscle regeneration. However, we observed high expression levels of human spectrin and lamin ac (**Figure 6m**) near the graft-host interface, which suggests that the regenerative potency of the implanted hiPSC-MPC laden constructs contributed to the promoted muscle regeneration in V3.

Our study showed angiogenesis and vascular invasion of the implanted vascularized constructs into the host tissue. As shown in **Figure 6n** (same cross-sectional area shown in 6j-2) and **Figure 6o**, human vasculature (expressing CD31) was prevalently found among murine vasculature near the scaffold interface and the surrounding host tissue, as well as in the V2 control group (**Figure S24b(iii)**). This is in line with the subcutaneous study (**Figure 5i**) where both the human and the murine ECs were observed at the implant site. Consequently, the expression of ECs from both human and murine species at the injury site after four weeks of *in vivo* culture suggests that the fabricated muscle constructs are capable of homing in host tissue cells. Moreover, strong expression of βIII-tubulin (TUJ1) at the host-scaffold interface (**Figure 6p**) and the surrounding tissue (**Figure 6q**) suggests that the constructs could support integration with host motor or sensory neurons, which, as previously reported, can enhance myocyte fusion and can support the formation of functional neuromuscular junctions.[3] TUJ1 expression was relatively lower in the V2 control group (**Figure S24b(iv)**). These results were conclusively observed in bilateral scaffold implants in both legs of the mice (**Figure S24c**). hiPSC-MPCs secrete vascular endothelial growth factor (VEGF), and cytokines which contribute to angiogenesis and accelerate the host's response to injury.[69,70] We measured VEGF secretion in a medium supernatant of *in vitro* cultured hiPSC-MPC-laden 3D bioprinted constructs (**Figure 6r**). These constructs contained hollow channels but were not coated by HUVECs. We observed a 3-fold increase in VEGF secretion over the course of the

second to third week after the induction of hiPSC-MPC differentiation, which contributed to axonal growth, angiogenesis and later muscle regeneration over the course of the *in vivo* study.[71-75] Overall, the vascularized hiPSC-MPC laden muscle constructs showed increased muscle regeneration, angiogenesis and maintenance of potent stem cells compared to control groups (V2 and V1). Together, these results provide a VML repair strategy based on pre-vascularized large-scale hiPSC-derived skeletal muscle implants.

Conclusion

This work pioneered a combination of biofabrication and stem cell technologies for the engineering of large pre-vascularized muscle fiber bundles. Specifically, we used EMB with sacrificial and photo-crosslinkable materials within a self-healing supporting gel matrix, which provided an interesting opportunity to fabricate complex features. The muscle fiber bioink was optimized for the 3D culture of iPSC-MPCs, a unique feat which was further supported by the capacity of this bioink to differentiate and mature these cells into skeletal myofiber bundles. Endowing the construct with endothelialized perfusable channels was of vital importance for sustaining the viability and function of muscle (stem) cells *in vitro* and *in vivo*, while also promoting graft-host integration. The 3D pre-vascularized tissue construct with hiPSC-MPCs was successfully implanted in a VML-injured animal model and demonstrated significantly higher cell survival in pre-vascularized bioprinted constructs compared with bulk constructs. By combining hiPSC-MPCs and a novel variant of EMB technology, this work provides a concrete step towards the engineering of large cell-laden muscle tissue constructs for VML repair strategies. Furthermore, the advanced biofabrication approach could potentially provide a feasible strategy towards high-throughput fabrication of high-fidelity biomimetic tissue constructs.

Declarations

Acknowledgement

This paper was funded by the National Institutes of Health (R01AR074234, R21EB026824, R01AR073822) and the Gillian Reny Stepping Strong Center for Trauma Innovation at Brigham and Women's Hospital. TK acknowledges funding from a Rubicon grant (019.183EN.017) by the Netherlands Organization for Scientific Research (NWO). We would like to thankfully acknowledge the contribution of the following researchers to this study: Aram Akbarzadeh, Atousa Nourmahnad, Dr. Guillermo Ulises Ruiz-Esparza, Prof. Belén Torres Barreiro, Eder Luna, Luis García Rivera, and Prof. Hassan Anwarul.

The authors declare no conflict of interest.

Author Contributions

S.R.S. conceived, designed, and coordinated the study. S.R.S., Y.A.J. and T.Z. designed, planned, and conducted in vitro and in vivo experiments, as well as analyzing and interpreting the data and writing the manuscript. Z.A.T. cultured hiPSCs into hiPSC-MPCs and advised on optimizing experiments and interpreting results. T.K. contributed to in vitro data analysis and manuscript drafting and revision. I.S., A.T., O.P. supervised parts of the experiments and provided technical support on experiment data and findings. K.S., Y.K., J.Q., A.A., K.K., S.H., J.L., A.F.H.M., S.L.O., K.L., M.A.C. and A.C. contributed to parts of experiments and data analysis, particularly to in vitro characterization. A.C.P., Y.E. and X.W. conducted animal surgeries. All authors had the opportunity to comment on the paper.

Data availability

The datasets generated during and/or analyzed during the current study are available from the corresponding author on reasonable request.

Experimental Section

Materials

The following were purchased from Sigma Aldrich: Gelatin from porcine skin, 2-hydroxy-4'-(2-hydroxyethoxy)-2-methylpropiophenone (photo-initiator (PI), Irgacure D-2959) and methacrylic anhydride (MA). The following were purchased from Thermo Fisher Scientific: phosphate buffered saline (PBS) and Hanks' balanced salt solution (HBSS). Following previous GelMA synthesis protocols, we synthesized medium degree GelMA[76] by administering 5% (v/v) MA to the gelatin mix at a 0.5 ml/min mixing rate. EBM™-2 Basal medium with an EGM™-2 SingleQuots™ supplement of growth factors (Lonza) was used for HUVEC cell culture and channel ink preparation (HUVEC media).

Embedded multi-material (EMB) bioprinting of 3D constructs

To prepare the supporting matrix, molds were fabricated with polydimethylsiloxane (PDMS) and sterilized using 70% ethanol, overnight UV exposure in the biosafety cabinet, and sterile PBS washing. Next, 0.25 wt% PI and 5 wt% freeze-dried GelMA were mixed in 40% HBSS and 60% hiPSC-MPC proliferation medium and the solution was incubated for 1 hour at 37 °C (GelMA pre-polymer solution). Next, the solution was poured into the mold, and was allowed to gelate (sol-gel state) at 4 °C for ~5-8 minutes.

The muscle bioink was prepared with 7.5% GelMA, 2 wt% gelatin and 0.25% PI dissolved in HBSS and hiPSC-MPC proliferation medium (2:3) and was followed by a 1-hour incubation step at 37 °C. At the time of bioprinting, a pellet of hiPSC-MPCs was uniformly dissolved in 600 µl bioink prepolymer solution to make the bioink, which was then transferred to a 1ml syringe with a printhead needle (30G, blunt, BD). 3D bioprinting was performed using a Cellink Inkredible bioprinter that was calibrated prior to each run with respect to the positional accuracy of the needle and a reference mold in XYZ directions. In the case of dual ink printing, the second nozzle (perfusable channel ink) was also calibrated in reference to the muscle ink nozzle. The muscle ink was extruded at a 4 µl/min rate using an *ad hoc* syringe pump (New Era Pump Systems). To create perfusable channels, a soluble 5% gelatin ink was prepared and printed inside the bath in the form of highly aligned channels. To ensure the printability of the ink, gelatin was thermally gelated and printed at 19-22 °C. Next, the GelMA construct with bioprinted hiPSC and gelatin channels were exposed to a UV light source (~100 mW cm^{-2}, OmniCure S2000) to be chemically crosslinked. Constructs were then taken out from the molds, and were washed (PBS) and collected onto a 24-well plate pre-filled with warm hiPSC-MPC proliferation medium, followed by incubation at 37 °C and 5% CO_2. The media was changed after 1 hour to remove the dissolved gelatin from the constructs. The medium was refreshed on day 1 after printing and regularly every 2 days afterwards, until the differentiation medium was changed, or until fixation or implantation of the constructs. By submerging the constructs in medium and incubating the construct at 37°C, the gelatin inside the printed channels gradually dissolved into the solution, leaving a fully hollow channel inside the crosslinked GelMA bath.

For bioprinting the muscle flap geometries, a CAD drawing of each geometry was used to laser-cut and create customized PDMS molds. Next, a 3D gcode was created using the Cellink Heartware software. An appropriate angle of printing was chosen such that the ratio of Z travel to X travel (and Z travel to Y travel) remained larger than 1. The mold was cut open and the nozzle traveled in the Z direction to bioprint the structure. The construct was then bioprinted and crosslinked under UV light using the parameters mentioned above.

To extrude multi-material coaxial filaments, a coaxial nozzle was fabricated by adhering concentric 25G inner and 18G outer needles using hot glue. To bioprint the sheath, 5% GelMA and 2% alginate was fed into the outer needle at 16 µl/min. To bioprint the core, 5% GelMA and 2% gelatin supplemented with 0.25% PI and 1% $CaCl_2$ was fed to the inner needle at 8 µl/min. The core-sheath crosslinking was achieved through the Ca^{2+} crosslinking of alginate as well as GelMA covalent gelation upon UV irradiation.

Characterization of mechanical and rheological properties

To perform compression mechanical tests on the constructs (cylindrical samples, diameter = 0.9 cm, height = 0.5 cm), a parallel plate platform was used to compress the samples at room temperature until

rupture (ADMET, MTESTQuattro). The linear portion of the resulted stress-strain curve (i.e., <20% strain) was used to calculate the Young's modulus.

Cyclic compression tests were performed and recorded on an Instron 5966 Universal Testing System with 500 N load cell. To ensure symmetry, the constructs were 3D bioprinted in the same cylindrical molds as mentioned above and were cut in half (perpendicular to the bioprinted channels). 2 mm sample cuts showed nearly identical results. Five cycles (0-10% strain) were performed sequentially to ensure good contact and the absence of hysteresis. Then, incremental strain ranges were used to perform sequential cyclic tests (starting at 0% strain, going up to 10%, 20%, 30%, and 40%), returning to 0% strain in between the increments. To ensure reproducibility, the strain incremental measurement was repeated for one sample and an excellent agreement was obtained.

To measure the rheological properties of the bioinks (Anton Paar MCR 302 rheometer), a 10-millimeter diameter concentric cylinder Couette DIN bob with a 10.84 mm diameter cup (~1 mL sample volume) was used for all measurements, giving a geometry gap between the inner and outer cylinders of 0.42 mm. This geometry was selected to minimize the impact of drying and to increase the surface area to obtain a better signal than possible via a parallel plate or cone and plate geometry. A C-PTD200 module (bottom), chiller (Julabo circulating chiller) and solvent trap attachments (Anton Paar) were used to maintain temperature control. Experimental data recording and analysis were performed with Anton Paar RheoCompass. Temperature sweeps were done between 4 and 37 ºC; all samples were allowed to equilibrate for at least 10 minutes at 4 ºC prior to measurement. For oscillatory temperature ramps, the ramp rate was 1 ºC/min; the strain amplitude and frequency were γ_0 = 0.3% and ω=10 rad/s, respectively, chosen to be in the linear viscoelastic regime (LVE) at 4 ºC determined by amplitude sweeps. The sweep was then reversed to examine rheological hysteresis. Before each sample measurement, calibrations were done to the measuring system inertia of the upper plate, as well as the motor that compensated for residual friction. Next, after gap recalibration, the constructs were introduced to the machine and were allowed to reach an equilibrium before running the test (10 minutes).

Characterization of microporous structures of hydrogels

To perform SEM imaging, the constructs were first incubated in PBS overnight at 37 ºC. The constructs were then collected and freeze-dried inside 1 ml Eppendorf tubes that were punctured on the cap for air release. Next, the constructs were cut at different horizontal and vertical cross-sections parallel or perpendicular to the bioprinted channels. SEM imaging was performed at the Harvard center for nanoscale systems.

Characterization of perfusable microchannels

To characterize the perfusability of the hollow channels, a perfusion test was performed using FITC-Dextran dye. Briefly, 5% FITC-Dextran powder was dissolved in PBS and covered by aluminum foil. The constructs were first placed horizontally (channels were oriented parallel to the ground) on a petri dish on a confocal microscope and a stacked image (image 0) was captured from the channels using the brightfield channel and the green fluorescent laser. Next, the constructs were gently flipped vertically (channels were now oriented vertically) and 10 µl of the FITC solution was added to the channels from the top. The constructs were immediately flipped over to the initial orientation, and the diffusion was recorded using the time series function of the confocal microscope in a 20-minute span. Stacked images of the green fluorescent laser and brightfield were recorded every 10 minutes. The images were then analyzed using ImageJ to calculate fluorescence intensity near the channels. To calculate the diffusional permeability, the following formula was used following a previous protocol[45]:

$$P_d = \frac{1}{l_1 - l_b}\left(\frac{l_2 - l_1}{t}\right)\frac{d}{4}$$

Where P_d represented the diffusional permeability, I_1 was the average intensity at image 0, I_2 was the average intensity in the later timepoints (e.g. t ~10 min), I_b was the background intensity before FITC addition, and d was the diameter of the printer channel (~345 µm). The portion of the intensity curve on the left side of the peak was used to calculate the fluorescent intensity.

Cell culture and differentiation

Culture of HUVECs: Human Umbilical Vein Endothelial Cells (HUVECs) with prescreened angiogenesis were purchased from Lonza. Cells were cultured in EBM™-2 Basal medium supplemented with EGM™-2 pre and post printing.

Derivation and culture of hiPSC-MPCs: The NCRM1 hiPSCs were cultured according to previous procotols.[33] Briefly, Matrigel-coated plates (BD) were used to seed and culture the cells using mTesR1 medium (Stem Cell Technologies). Aggregate and single-cell passaging could both be used. The cells were verified free of mycoplasma. hiPSC-derived myogenic progenitors were generated following a serum-free differentiation method.[11,47] Three- to four-week-old wild-type hiPSC-derived primary myogenic populations were detached to replate (cell density = 3.5-4 x 10^4 cm^2) myogenic progenitors on Matrigel-coated plates (Corning) and the cells were then cultured in skeletal muscle growth medium (SKGM-2, Lonza) supplemented with 10 µM ROCK inhibitor for 24 hours. Afterwards, the ROCK inhibitor was

removed and the culture was continued with SKGM-2 for ~2 days until they were dissociated using Accutase (Stemcell Technologies) and were frozen or prepared for bioprinting.

Preparation of hiPSC-MPCs for 3D bioprinting: 2 days prior to 3D bioprinting, frozen vials of hiPSC-MPCs were thawed and seeded onto Matrigel-coated 6-well plates (Matrigel hESC-qualified, Corning). Specifically, the cells were thawed, resuspended in SKGM-2+Ri medium (SKGM-2+Ri (10 µM) + 0.2% Pen/Strep) and were seeded at a density of $8*10^4$ cells /cm^2. The medium was replaced with SKGM-2+0.2% P/S after 24 hours and until bioprinting.

Differentiation of hiPSC-MPCs: To differentiate *h*iPSC-MPCs into skeletal muscle cells, a medium cocktail of the following components was used (iPSC-Diff media) following a previously established hiPSC-MPC differentiation protocol[11]: Briefly, after 24-48 hours, cells were induced for myogenic differentiation in DMEM/F-12, GlutaMAX™ (Gibco) supplemented with 1 µM Chiron (Tocris), 2% knock-out serum replacement (KSR, Invitrogen), 0.2% Pen/Strep (Life Technologies), Insulin-Transferrin-Selenium (ITS, Life Technologies), and 10 µM TGF-β inhibitor SB431542 (Tocris, KCTi). After differentiation induction, medium was refreshed every day until day 2 and afterwards, every other day.

Culture and differentiation of C2C12s: Mouse C2C12 cells were purchased from ATCC (CRL-1772) and were cultured and maintained following the vendor protocol. To differentiate C2C12s into skeletal muscle cells, the application of proliferation medium (Dulbecco's modified Eagle medium (DMEM), 10% FBS, 1% P/S) was stopped and DMEM supplemented with 2% horse serum (Gibco) and 1% P/S was used to induce differentiation and continue culture by refreshing the medium every other day.

Fabrication of cell-laden bulk hydrogels

HUVEC-laden GelMA constructs: To fabricate bulk hydrogels containing embedded HUVECs, 5% GelMA bath pre-polymer solution was prepared as explained in the previous sections. Next, HUVECs were trypsinized and the pellet was resuspended in the pre-polymer solution to reach a final cell density of 7.5 x 10^6 cells/ml. Next, the pre-polymer solution was poured into PDMS molds as explained above and incubated in 4 ºC for 5-8 minutes. The constructs were then crosslinked under UV light (100 mW/cm^2) for 55 seconds, and were extracted from the molds, washed with PBS and placed in 24-well plates supplemented with HUVEC culture medium. The medium was refreshed 1 hour after crosslinking, the day after, and after that regularly every 2 days.

iPSC-MPC-laden GelMA: To fabricate bulk hydrogels containing embedded hiPSC-MPCs, 7.5% GelMA bath pre-polymer solution containing 0.25% PI was prepared in a solution containing 40% HBSS and 60% SKGM-2+Ri medium. hiPSC-MPCs were trypsinized and embedded in this pre-polymer solution at a density of 7.5 million cells/ml. Next, the pre-polymer solution containing cells was poured into PDMS molds and incubated at 4 ºC for 5-8 minutes. The constructs were next crosslinked under UV light (100

mW/cm^2) for 55 seconds, and were extracted from the molds, washed with PBS and placed in 24-well plates supplemented with SKGM-2+Ri culture medium. The medium was refreshed 1 hour after crosslinking, the day after, and then regularly every 2 days.

Fabrication of 3D vascularized (HUVEC-seeded) constructs

5% soluble gelatin ink was first prepared according to the soluble ink preparation instructions. Next, cells were trypsinized and centrifuged for 5 minutes at 1000 rpm. Afterwards, HUVECs were added to the ink at a density of 4 x 10 ^{7} cells/ml. Meanwhile, the media of the wells containing constructs was aspirated by pipette. Constructs were placed vertically using a small spatula in 48-well plates. 10 µL of HUVEC-laden bioink (4 x 10^5 cells) were injected two times on top of each construct through the cross section of the hollow channels using a pipette. Constructs were immediately flipped on the side. After adding cells to all constructs, the well plate was returned to the incubator for 45 minutes to allow cells to loosely attach to the wall. At this time, no media was added to the constructs. After this incubation period, the constructs were placed vertically again and another two rounds of 10 µL HUVEC-laden bioink were injected inside all channels in each construct. Constructs were again flipped horizontally and incubated for 45 minutes at 37°C. After this time, constructs were checked under the microscope to confirm the presence of cells inside the channels. HUVEC media was gently added to each construct and the constructs were incubated overnight. The media was changed the next day to avoid possible contaminations. The constructs were replated in new 48-well plates after 2-3 days to avoid consumption of media by the cells that might have migrated to the bottom of the well plate.

Characterization of in vitro cultured samples

Fixation of cell-laden constructs was done at different timepoints (e.g. day 10, day 20, day 30). Briefly, the constructs were treated with 4% paraformalehyde solution (Thermo Fisher scientific) for 20 minutes. Next, the constructs were treated with 0.1% Triton-X 100 for 10 min, and then washed with DPBS three times. The constructs were next blocked with 10% goat serum in DPBS for 1 hour at 25°C. To stain the cytoskeleton, F-actin (1:40, Invitrogen) was added to the constructs. Primary antibodies that were used in this study included mouse anti- myoG (DHSB, F5D-C), mouse anti-myogenin (Developmental Studies Hybridoma Bank, F5D, 1:200) mouse anti-Pax7 (Developmental Studies Hybridoma Bank, 1:100), mouse anti-beta-III tubulin monoclonal antibody (anti-β III tubulin, 1:500, Abcam), mouse anti-human spectrin (Leica, NCL-SPEC1, 1:100), rabbit anti-human lamin A/C (Abcam, ab108595, 1:50) and mouse anti fast myosin heavy chain (Monoclonal Anti-Myosin (Skeletal, Fast) antibody produced in mouse, MY-32, 1:100, sigma-aldrich). To stain the HUVECs, CD31 antibody (1:100, DSHB) was used. Conjugated secondary antibodies (goat anti-mouse IgG, Invitrogen Alexa Fluor 594, Thermo Fisher, 1:200) were added

and the constructs were incubated at 4 °C for 6 hours. DAPI (1:1000, Sigma-Aldrich) was added 30 minutes prior to imaging and was used for visualization. For imaging the constructs, a fluorescence (Zeiss Axio Observer D1) and a confocal microscope (SP7, Leica) were employed. To acquire Z-stack, tiled and time-lapse 3D images (e.g. the endothelialized constructs and the dye diffusion tests), a Zeiss LSM 880 airyscan confocal microscope was used. Image processing and data analysis of the stacked data was performed using Zen Blue and Fiji.

Fast Fourier transform (FFT) analysis

To quantify the extent of muscle fiber alignment, FFT analysis was performed using a previously described method[77]. Briefly, the images were stored and analyzed as uncompressed .TIFF files and were converted to grayscale 8-bit images. ImageJ was used to conduct 2D FFT analysis on four images per print condition. The obtained image was then analyzed using a MATLAB program we developed to plot the FFT alignment intensity versus angle or orientation in degrees. From each orientation histogram, the angle at which most fibers were aligned was determined. Alignment index was calculated as the fraction of cells aligned within 20º of the peak angle.[78] The larger the alignment index was, the higher was the fraction of fibers aligned near a peak angle. A completely randomly aligned matrix was indicated by an alignment index of 0.

In vivo subcutaneous study

HUVEC-laden constructs cultured for 3-4 weeks were selected for implantation. Four groups of constructs containing HUVECs were fabricated as below:

G1 - *Endothelialized perfusable channels in the supporting bath*: perfusable channels were fabricated in a 5% GelMA supporting bath as described in the previous sections. The channels were later seeded with HUVECs and cultured for 2 weeks before surgery.

G2 - *Endothelialized perfusable channels in the HUVEC-laden supporting bath*: HUVEC-laden bulk GelMA pre-polymer solution was prepared as previously described. This bath was used to 3D bioprint perfusable channels according to the protocol described previously.

G3 - *Perfusable channels in the supporting bath.* This group did not contain any cells and was bioprinted as a control group for G1. Briefly, perfusable channels were bioprinted in a 5% GelMA bath as described previously. The constructs were cultured for 2 weeks before surgery.

G4 - *HUVEC-laden supporting bath.* This group contained a bulk cell-laden hydrogel with no 3D bioprinting involved. The constructs were prepared according to the protocol described above for fabricating bulk hydrogels. The constructs were cultured for 2 weeks before surgery. This group served as a control group for G2, investigating the effect of incorporating bioprinted perfusable channels in the constructs.

All animal procedures were approved by the Institutional Animal Use and Care Committee of Harvard Medical School (Protocol number: 2017N000114). 12-week-old nude rats (Charles River) were acclimatized for a week prior to surgery in the vivarium of Brigham and Women's Hospital. Subcutaneous embedding test was performed on nude rats anesthetized with Isoflurane anesthetic. Briefly, subcutaneous space was accessed through dorsal incision with the length of 2 cm. Subsequent subcutaneous pockets were created by blunt separation. Next, three hydrogel constructs were introduced into the subcutaneous pockets on bilateral sides of the cut. Total of 6 constructs were implanted for each group. To alleviate post-surgery pain of rats, carprofen (5 mg/kg BW/day s.c. as a single injection) was postoperatively administered for 72 hours and the rats were monitored hourly for 6 hours post-surgery and twice per day for 5 days. Samples of each group were harvested at two timepoints (weeks 1 and 4). The implanted gels and surrounding tissue were removed for further staining and studying angiogenic properties. Next, the harvested cell-laden printed constructs were washed with PBS and fixed in 4% paraformaldehyde for 24 hours before staining with Haemotoxylin and Eosin (H&E) and human-specific and rat-specific CD31 antibodies (iHisto.io).

Fabrication and characterization of suturable PGS/PCL scaffolds

PGS Synthesis: Poly(glycerol sebacate) (PGS) was synthesized using an established protocol.[79] Equimolar quantities of sebacic acid (Sigma-Aldrich) and glycerol (Fisher Scientific) were mixed using a magnetic stirrer. The mixture was reacted under microwave radiation in 1 minute intervals for a total of 7 minutes at 500 W (Hamilton Beach, VA). After every minute interval, the microwave door was opened for 10 seconds to allow vapors to be removed. The synthesized PGS was allowed to cool to room temperature.

PGS/PCL Scaffold fabrication: Polycaprolactone (PCL) Mn 80,000 (Sigma-Aldrich) was dissolved at 20% (w/v) in hexafluoroisopropanol (HFIP) (CovaChem, IL) using a magnetic stirrer in a covered container to prevent evaporation. In a separate covered container, the synthesized PGS was dissolved in HFIP at 20% (w/v). Equal volumes of the PGS and PCL solutions were added together and mixed on a magnetic stirring for 3 hours at room temperature. The solution was transferred to a syringe and electrospun at 18 kV using a 22 G blunt-tipped needle. The fibers were collected on a rotating drum coated with aluminum foil. The drum was rotated at a speed of 50 rpm and set at a distance of 22 cm from the tip of the needle. The electrospun mats and aluminum foil were removed from the drum and desiccated for 24 hours.

Preparation and sterilization of scaffolds for surgery: On the day before surgery, PGC/PCL scaffolds were sterilized with 70% ethanol and were left inside the biosafety cabinet overnight. On the day of the surgery, the scaffolds were detached from the foil gently using two forceps inside the biosafety cabinet. The bioprinted constructs were attached to the scaffolds by adding a drop (~15µL) of GelMA prepolymer solution (7.5% GelMA+ 0.5% PI) to the mesh and placing the constructs on top of the pre-polymer solution. The constructs were crosslinked under UV light (100 mW/cm^2) for 5 seconds. The adhesion of construct-mesh makeup was tested by applying tensile forces to the construct with forceps. Next, the constructs attached to the mesh were placed in 48-well plates, supplied with SKGM-2 medium and incubated at 37 ºC until surgery.

Mechanical characterization of PGS/PCL scaffolds: Using a surgical suture, 20mm x 6mm x 0.1mm rectangular shaped specimens of the PGS/PCL scaffold were sutured. The tensile strength of both the sutured and non-sutured scaffolds were studied using a uniaxial material testing system (Instron 3342). Rectangular-shaped specimens (40mm x 6mm x 0.1mm) were stretched at a strain rate of 7mm per minute, in compliance with the ASTM D822 standard. Five samples were tested for each group. The Young's modulus 'E' of the fibers was calculated from the linear region of the stress-strain curve corresponding to 0%-30% of the tensile strain.

Morphological characterization of PGS/PCL scaffolds: Electrospun PGS/PCL sheets were imaged using scanning electron microscopy. First, desiccated sheets were coated in platinum and palladium for 10 seconds using a Sputter Coater 108 Auto (Cressington, UK). The coated sheets were imaged on a high vacuum at 2 kV using a FEI Quanta 200 ESEM (FEI Company, Hillsboro, OR). To image scaffold-hydrogel interfaces, a 1cm^2 piece of the PGS/PCL scaffold was photo-crosslinked on a polymerized GelMA hydrogel cube. The scaffold was pre-wet with liquid GelMA before putting on the hydrogel cube and crosslinked with a UV light for 20 seconds operating at 850 mW/cm^2 intensity. The PGS/PCL-GelMA construct was freeze-dried for 3 days. The samples were sputter-coated with a 5nm thin layer of Pt/Pd alloy (80:20) for increased conductivity and imaged using JEOL JSM-IT100 InTouchScope™ scanning electron microscope operated at an accelerated voltage of 5-10 kV. Fiber diameters of the scaffold and pore sizes of the GelMA hydrogel were measured using Image J software. Three samples were analyzed, and 10 images taken from different areas of the cross-section.

In vivo VML study

All animal procedures were approved by the Institutional Animal Use and Care Committee of Harvard Medical School (Protocol number: 2016N000375). 8-week-old mice (Jackson Laboratories; Bar Harbor, ME, USA) were acclimatized for a week prior to surgery in the vivarium of Brigham and Women's Hospital. Four NOD-*scid* IL2Rgamma^{null} mice and two C57BL6J WT mice were used in this study for the iPSC-laden and acellular hydrogel implants, respectively. Mice were anaesthetized using a 2-4% isoflurane

vaporizer induction chamber and the surgical site was disinfected with chlorhexidine and 70% isopropanol (Contec, Spartanburg, SC).

The mice were divided into three equal groups: VML treated with 3D vascularized muscle tissue (V3), VML treated with acellular bioprinted constructs (V2) and untreated VML (V1). Bilaterally, a longitudinal incision at quadriceps muscle was created followed by a sharp resection of the quadriceps muscle in parallel to the femur length. Following a prior protocol, in all study groups, approximately 34.7 ± 0.7 mg of the muscle was cut, leaving only a base of the skeletal muscle.[80] In the groups receiving treatment (V3 and V2), the construct (acellular bioprinted or vascularized muscle tissue) was attached to a PGS/PCL scaffold and placed with the scaffold side up bilaterally into the VML defects. The skin incision was closed in all groups using 4–0 Prolene suture (Ethicon Inc, Somerville, NJ). To represent the remodeling phase of muscle healing, the hind limb quadriceps muscles of the mice were harvested four weeks post-surgery and fixed in 10% formalin followed by 70% ethanol for histological analysis.

Characterization of in vivo cultured samples

After implantation, the constructs were incubated in 10% formalin solution for 48 hours followed by storage in 70% alcohol in 4 ºC. Histological analysis and immunostaining were performed afterwards by iHisto.io company. For VML studies, MyHC (Monoclonal Anti-Myosin (Skeletal, Fast) antibody produced in mice, MY-32, 1:100, sigma-aldrich), Pax7 (1:80, DSHB), DAPI, MYH3 (Rabbit polyclonal to heavy chain Myosin/MYH3, 1 µg/ml, Abcam), TUNEL, βIII-tubulin (Rabbit polyclonal to beta III Tubulin, 1:500, Abcam), Lamin A/C (Rabbit Anti-Lamin A+ Lamin C, 1:500, Abcam), and Spectrin (Mouse Monoclonal Antibody Spectrin, 1:100, Leica) were used. For subcutaneous studies, anti-mouse and anti-human CD31 antibodies were used, as provided by iHisto.io. H&E staining was also performed by the company on both VML and subcutaneous studies.

Statistical analysis

Statistical analysis of the data was performed using GraphPad Prism. Tukey's multiple comparisons, Sidak's multiple comparisons, Mann-Whitney test and unpaired t-test were used to compare the data groups of *in vitro* and *in vivo* experiments. The p-values, number of samples (n), and the type of each analysis are provided in the figure captions of the corresponding graphs.

References

1 Grogan, B. F. & Hsu, J. R. Volumetric muscle loss. *J Am Acad Orthop Surg* **19 Suppl 1**, S35-37 (2011).

2 Sun, Y., Deng, R., Ren, X., Zhang, K. & Li, J. 2D Gelatin Methacrylate Hydrogels with Tunable Stiffness for Investigating Cell Behaviors. *ACS Applied Bio Materials* **2**, 570-576, doi:10.1021/acsabm.8b00712 (2019).

3 Das, S. *et al.* Pre-innervated tissue-engineered muscle promotes a pro-regenerative microenvironment following volumetric muscle loss. *Communications biology* **3**, 1-14 (2020).

4 Harris, B. N. & Bewley, A. F. Minimizing free flap donor-site morbidity. *Current Opinion in Otolaryngology & Head and Neck Surgery* **24**, 447-452 (2016).

5 Larouche, J., Greising, S. M., Corona, B. T. & Aguilar, C. A. Robust inflammatory and fibrotic signaling following volumetric muscle loss: a barrier to muscle regeneration. *Cell death & disease* **9**, 1-3 (2018).

6 Buchanan, S. M. *et al.* Pro-myogenic small molecules revealed by a chemical screen on primary muscle stem cells. *Skeletal muscle* **10**, 1-14 (2020).

7 Kim, J. H. *et al.* Neural cell integration into 3D bioprinted skeletal muscle constructs accelerates restoration of muscle function. *Nature communications* **11**, 1-12 (2020).

8 Machida, S., Spangenburg, E. E. & Booth, F. W. Primary rat muscle progenitor cells have decreased proliferation and myotube formation during passages. *Cell Proliferation* **37**, 267-277, doi:10.1111/j.1365-2184.2004.00311.x (2004).

9 Rinaldi, F. & Perlingeiro, R. C. R. Stem cells for skeletal muscle regeneration: therapeutic potential and roadblocks. *Translational Research* **163**, 409-417, doi:https://doi.org/10.1016/j.trsl.2013.11.006 (2014).

10 del Carmen Ortuño-Costela, M., García-López, M., Cerrada, V. & Gallardo, M. E. iPSCs: A powerful tool for skeletal muscle tissue engineering. *Journal of cellular and molecular medicine* **23**, 3784-3794, doi:10.1111/jcmm.14292 (2019).

11 Chal, J. *et al.* Generation of human muscle fibers and satellite-like cells from human pluripotent stem cells in vitro. *Nature protocols* **11**, 1833-1850, doi:10.1038/nprot.2016.110 (2016).

12 Rao, L., Qian, Y., Khodabukus, A., Ribar, T. & Bursac, N. Engineering human pluripotent stem cells into a functional skeletal muscle tissue. *Nat Commun* **9**, 126, doi:10.1038/s41467-017-02636-4 (2018).

13 Biressi, S., Molinaro, M. & Cossu, G. Cellular heterogeneity during vertebrate skeletal muscle development. *Dev Biol* **308**, 281-293, doi:S0012-1606(07)01122-0 [pii]

10.1016/j.ydbio.2007.06.006 (2007).

14 Aubin, H. *et al.* Directed 3D cell alignment and elongation in microengineered hydrogels. *Biomaterials* **31**, 6941-6951, doi:10.1016/j.biomaterials.2010.05.056 (2010).

15 Ahadian, S. *et al.* Interdigitated array of Pt electrodes for electrical stimulation and engineering of aligned muscle tissue. *Lab Chip* **12**, 3491-3503, doi:10.1039/c2lc40479f (2012).

16 Quarta, M. *et al.* An artificial niche preserves the quiescence of muscle stem cells and enhances their therapeutic efficacy. *Nat Biotechnol* **34**, 752-759, doi:10.1038/nbt.3576 (2016).

17 Rouwkema, J., Koopman, B., Blitterswijk, C., Dhert, W. & Malda, J. Supply of nutrients to cells in engineered tissues. *Biotechnol Genet Eng Rev* **26**, 163-178, doi:10.5661/bger-26-163 (2010).

18 Rodriguez, B. L., Florida, S. E., VanDusen, K. W., Syverud, B. C. & Larkin, L. M. The maturation of tissue-engineered skeletal muscle units following 28-day ectopic implantation in a rat. *Regenerative engineering and translational medicine* **5**, 86-94 (2019).

19 Nakayama, K. H. *et al.* Treatment of volumetric muscle loss in mice using nanofibrillar scaffolds enhances vascular organization and integration. *Communications biology* **2**, 1-16 (2019).

20 Song, W. *et al.* Engineering transferrable microvascular meshes for subcutaneous islet transplantation. *Nature Communications* **10**, 4602, doi:10.1038/s41467-019-12373-5 (2019).

21 Zhang, B. & Radisic, M. Organ-level vascularization: The Mars mission of bioengineering. *The Journal of thoracic and cardiovascular surgery* **159**, 2003-2007, doi:10.1016/j.jtcvs.2019.08.128 (2020).

22 Vunjak-Novakovic, G. *et al.* Challenges in cardiac tissue engineering. *Tissue Engineering Part B: Reviews* **16**, 169-187 (2009).

23 Maffioletti, S. M. *et al.* Three-dimensional human iPSC-derived artificial skeletal muscles model muscular dystrophies and enable multilineage tissue engineering. *Cell reports* **23**, 899-908 (2018).

24 Compaan, A. M., Song, K., Chai, W. & Huang, Y. Cross-Linkable Microgel Composite Matrix Bath for Embedded Bioprinting of Perfusable Tissue Constructs and Sculpting of Solid Objects. *ACS Applied Materials & Interfaces* **12**, 7855-7868, doi:10.1021/acsami.9b15451 (2020).

25 Jeon, O. *et al.* Individual cell-only bioink and photocurable supporting medium for 3D printing and generation of engineered tissues with complex geometries. *Materials Horizons* **6**, 1625-1631, doi:10.1039/C9MH00375D (2019).

26 de Melo, B. A. G. *et al.* 3D Printed Cartilage-Like Tissue Constructs with Spatially Controlled Mechanical Properties. *Adv Funct Mater* **29**, 1906330, doi:10.1002/adfm.201906330 (2019).

27 Hinton, T. J. *et al.* Three-dimensional printing of complex biological structures by freeform reversible embedding of suspended hydrogels. *Sci Adv* **1**, e1500758, doi:10.1126/sciadv.1500758 (2015).

28 Bhattacharjee, T. *et al.* Writing in the granular gel medium. *Sci Adv* **1**, e1500655, doi:10.1126/sciadv.1500655

1500655 [pii] (2015).

29 Li, Y.-C. *et al.* Toward a neurospheroid niche model: optimizing embedded 3D bioprinting for fabrication of neurospheroid brain-like co-culture constructs. *Biofabrication* (2020).

30 Zhu, K. *et al.* Gold Nanocomposite Bioink for Printing 3D Cardiac Constructs. *Adv Funct Mater* **27**, doi:10.1002/adfm.201605352 (2017).

31 Blaeser, A. *et al.* Controlling Shear Stress in 3D Bioprinting is a Key Factor to Balance Printing Resolution and Stem Cell Integrity. *Advanced healthcare materials* **5**, 326-333, doi:10.1002/adhm.201500677 (2016).

32 Chal, J. *et al.* Generation of human muscle fibers and satellite-like cells from human pluripotent stem cells in vitro. *Nat Protoc* **11**, 1833-1850, doi:10.1038/nprot.2016.110 (2016).

33 Chal, J. *et al.* Differentiation of pluripotent stem cells to muscle fiber to model Duchenne muscular dystrophy. *Nat Biotechnol* **33**, 962-969, doi:10.1038/nbt.3297 (2015).

34 Russell, C. S. *et al.* In Situ Printing of Adhesive Hydrogel Scaffolds for the Treatment of Skeletal Muscle Injuries. *ACS Applied Bio Materials* **3**, 1568-1579 (2020).

35 McLoon, L. K., Vicente, A., Fitzpatrick, K. R., Lindström, M. & Pedrosa Domellöf, F. Composition, Architecture, and Functional Implications of the Connective Tissue Network of the Extraocular Muscles. *Investigative ophthalmology & visual science* **59**, 322-329, doi:10.1167/iovs.17-23003 (2018).

36 Kuang, S., Kuroda, K., Le Grand, F. & Rudnicki, M. A. Asymmetric self-renewal and commitment of satellite stem cells in muscle. *Cell* **129**, 999-1010, doi:10.1016/j.cell.2007.03.044 (2007).

37 Yin, J., Yan, M., Wang, Y., Fu, J. & Suo, H. 3D Bioprinting of Low-Concentration Cell-Laden Gelatin Methacrylate (GelMA) Bioinks with a Two-Step Cross-linking Strategy. *ACS Applied Materials & Interfaces* **10**, 6849-6857, doi:10.1021/acsami.7b16059 (2018).

38 Rastin, H., Ormsby, R. T., Atkins, G. J. & Losic, D. 3D Bioprinting of Methylcellulose/Gelatin-Methacryloyl (MC/GelMA) Bioink with High Shape Integrity. *ACS Applied Bio Materials* **3**, 1815-1826, doi:10.1021/acsabm.0c00169 (2020).

39 Tamayol, A. *et al.* Hydrogel Templates for Rapid Manufacturing of Bioactive Fibers and 3D Constructs. *Advanced healthcare materials*, doi:10.1002/adhm.201500492 (2015).

40 Rouwkema, J., Rivron, N. C. & van Blitterswijk, C. A. Vascularization in tissue engineering. *Trends in biotechnology* **26**, 434-441, doi:https://doi.org/10.1016/j.tibtech.2008.04.009 (2008).

41 Cristina, C. *et al.* Microfluidic bioprinting of heterogeneous 3D tissue constructs using low viscosity bioink. *Advanced Materials* **Accepted** (2015).

42 Kolesky, D. B., Homan, K. A., Skylar-Scott, M. A. & Lewis, J. A. Three-dimensional bioprinting of thick vascularized tissues. *Proc. Natl. Acad. Sci. USA* **113**, 3179-3184 (2016).

43 Kim, B. S., Gao, G., Kim, J. Y. & Cho, D. W. 3D Cell Printing of Perfusable Vascularized Human Skin Equivalent Composed of Epidermis, Dermis, and Hypodermis for Better Structural Recapitulation of Native Skin. *Advanced healthcare materials* **8**, e1801019, doi:10.1002/adhm.201801019 (2019).

44 Massa, S. *et al.* Bioprinted 3D vascularized tissue model for drug toxicity analysis. *Biomicrofluidics* **11**, 044109, doi:10.1063/1.4994708 (2017).

45 Kolesky, D. B., Homan, K. A., Skylar-Scott, M. A. & Lewis, J. A. Three-dimensional bioprinting of thick vascularized tissues. *Proc Natl Acad Sci U S A* **113**, 3179-3184, doi:10.1073/pnas.1521342113 (2016).

46 Engler, A. J., Sen, S., Sweeney, H. L. & Discher, D. E. Matrix Elasticity Directs Stem Cell Lineage Specification. *Cell* **126**, 677-689, doi:https://doi.org/10.1016/j.cell.2006.06.044 (2006).

47 Al Tanoury, Z. *et al.* Differentiation of the human PAX7-positive myogenic precursors/satellite cell lineage in vitro. *Development (Cambridge, England)* **147**, doi:10.1242/dev.187344 (2020).

48 Kim, J. H. *et al.* 3D Bioprinted Human Skeletal Muscle Constructs for Muscle Function Restoration. *Scientific Reports* **8**, 12307, doi:10.1038/s41598-018-29968-5 (2018).

49 Ostrovidov, S. *et al.* 3D Bioprinting in Skeletal Muscle Tissue Engineering. *Small* **15**, e1805530, doi:10.1002/smll.201805530 (2019).

50 Ebrahimi, M. *et al.* Enhanced skeletal muscle formation on microfluidic spun gelatin methacryloyl (GelMA) fibres using surface patterning and agrin treatment. *Journal of tissue engineering and regenerative medicine* **12**, 2151-2163, doi:10.1002/term.2738 (2018).

51 Chen, B. & Shan, T. The role of satellite and other functional cell types in muscle repair and regeneration. *J. Muscle Res. Cell Motil.*, 1-8 (2019).

52 Cooper, A., Jana, S., Bhattarai, N. & Zhang, M. Aligned chitosan-based nanofibers for enhanced myogenesis. *Journal of Materials Chemistry* **20**, 8904-8911, doi:10.1039/C0JM01841D (2010).

53 Negroni, E., Bigot, A., Butler-Browne, G. S., Trollet, C. & Mouly, V. Cellular Therapies for Muscular Dystrophies: Frustrations and Clinical Successes. *Human Gene Therapy* **27**, 117-126, doi:10.1089/hum.2015.139 (2015).

54 Chalchat, E. *et al.* Changes in the Viscoelastic Properties of the Vastus Lateralis Muscle With Fatigue. **11**, doi:10.3389/fphys.2020.00307 (2020).

55 Karami, M., Calvo, B., Zohoor, H., Firoozbakhsh, K. & Grasa, J. Assessing the role of Ca2+ in skeletal muscle fatigue using a multi-scale continuum model. *Journal of Theoretical Biology* **461**, 76-83, doi:10.1016/j.jtbi.2018.10.034 (2019).

56 Chaturvedi, R. R. *et al.* Patterning vascular networks in vivo for tissue engineering applications. *Tissue Eng Part C Methods* **21**, 509-517, doi:10.1089/ten.TEC.2014.0258 (2015).

57 Qin, M. *et al.* In situ inflammatory-regulated drug-loaded hydrogels for promoting pelvic floor repair. *Journal of Controlled Release* **322**, 375-389, doi:10.1016/j.jconrel.2020.03.030 (2020).

58 Landau, S. *et al.* Tropoelastin coated PLLA-PLGA scaffolds promote vascular network formation. *Biomaterials* **122**, 72-82, doi:10.1016/j.biomaterials.2017.01.015 (2017).

59 Choi, Y. H. *et al.* Gelatin-based micro-hydrogel carrying genetically engineered human endothelial cells for neovascularization. *Acta Biomaterialia* **95**, 285-296, doi:10.1016/j.actbio.2019.01.057 (2019).

60 Chiesa, I. *et al.* Endothelial cells support osteogenesis in an in vitro vascularized bone model developed by 3D bioprinting. *Biofabrication* **12**, 025013, doi:10.1088/1758-5090/ab6a1d (2020).

61 Tamayol, A. *et al.* Biodegradable elastic nanofibrous platforms with integrated flexible heaters for on-demand drug delivery. *Scientific Reports* **7**, 9220, doi:10.1038/s41598-017-04749-8 (2017).

62 Jeffries, E. M., Allen, R. A., Gao, J., Pesce, M. & Wang, Y. Highly elastic and suturable electrospun poly(glycerol sebacate) fibrous scaffolds. *Acta Biomater* **18**, 30-39, doi:10.1016/j.actbio.2015.02.005 (2015).

63 Nuutila, K. *et al.* Gene expression profiling of skeletal muscle after volumetric muscle loss. *Wound Repair and Regeneration* **25**, 408-413, doi:10.1111/wrr.12547 (2017).

64 Quarta, M. *et al.* Bioengineered constructs combined with exercise enhance stem cell-mediated treatment of volumetric muscle loss. *Nat Commun* **8**, 15613, doi:10.1038/ncomms15613 (2017).

65 Marcinczyk, M. *et al.* The Effect of Laminin-111 Hydrogels on Muscle Regeneration in a Murine Model of Injury. *Tissue Engineering Part A* **25**, 1001-1012, doi:10.1089/ten.tea.2018.0200 (2018).

66 Sicherer, S. T., Venkatarama, R. S. & Grasman, J. M. J. B. Recent trends in injury models to study skeletal muscle regeneration and repair. *Bioengineering* **7**, 76 (2020).

67 Cui, C.-Y. *et al.* Skewed macrophage polarization in aging skeletal muscle. *Aging Cell* **18**, e13032, doi:10.1111/acel.13032 (2019).

68 Roman, W. & Gomes, E. R. Nuclear positioning in skeletal muscle. *Seminars in Cell & Developmental Biology* **82**, 51-56, doi:10.1016/j.semcdb.2017.11.005 (2018).

69 Ansari, S. *et al.* Human Periodontal Ligament- and Gingiva-derived Mesenchymal Stem Cells Promote Nerve Regeneration When Encapsulated in Alginate/Hyaluronic Acid 3D Scaffold. *Adv Healthc Mater* **6**, doi:10.1002/adhm.201700670 (2017).

70 Quarta, M. *et al.* An artificial niche preserves the quiescence of muscle stem cells and enhances their therapeutic efficacy. *Nat Biotechnol* **34**, 752-759, doi:10.1038/nbt.3576 (2016).

71 Staels, W., Heremans, Y., Heimberg, H. & De Leu, N. VEGF-A and blood vessels: a beta cell perspective. *Diabetologia* **62**, 1961-1968, doi:10.1007/s00125-019-4969-z (2019).

72 Yamamoto, N. *et al.* VEGF and bFGF induction by nitric oxide is associated with hyperbaric oxygen-induced angiogenesis and muscle regeneration. *Scientific Reports* **10**, 2744, doi:10.1038/s41598-020-59615-x (2020).

73 Jia, W. *et al.* Glass-activated regeneration of volumetric muscle loss. *Acta Biomaterialia* **103**, 306-317, doi:10.1016/j.actbio.2019.12.007 (2020).

74 Fang, Z. *et al.* Enhancement of sciatic nerve regeneration with dual delivery of vascular endothelial growth factor and nerve growth factor genes. *Journal of Nanobiotechnology* **18**, 46, doi:10.1186/s12951-020-00606-5 (2020).

75 Bin, Z., Zhihu, Z., Jianxiong, M. & Xinlong, M. Repairing peripheral nerve defects with revascularized tissue-engineered nerve based on a vascular endothelial growth factor-heparin sustained release system. *Journal of tissue engineering and regenerative medicine* **14**, 819-828, doi:10.1002/term.3048 (2020).

76 Yue, K. *et al.* Synthesis, properties, and biomedical applications of gelatin methacryloyl (GelMA) hydrogels. *Biomaterials* **73**, 254-271 (2015).

77 Bajaj, P. *et al.* Patterning the differentiation of C2C12 skeletal myoblasts. *Integrative biology : quantitative biosciences from nano to macro* **3**, 897-909, doi:10.1039/c1ib00058f (2011).

78 Ng, C. P., Hinz, B. & Swartz, M. A. Interstitial fluid flow induces myofibroblast differentiation and collagen alignment in vitro. *Journal of cell science* **118**, 4731-4739, doi:10.1242/jcs.02605 (2005).

79 Mollazadeh-Moghaddam, K. *et al.* Fracture-Resistant and Bioresorbable Drug-Eluting Poly (glycerol Sebacate) Coils. **2**, 1800109 (2019).

80 Panayi, A. C. *et al.* A porous collagen-GAG scaffold promotes muscle regeneration following volumetric muscle loss injury. *Wound Repair and Regeneration* **28**, 61-74, doi:10.1111/wrr.12768 (2020).

81 O'Bryan, C. S. *et al.* Self-assembled micro-organogels for 3D printing silicone structures. *Science Advances* **3**, e1602800, doi:10.1126/sciadv.1602800 (2017).

Figures

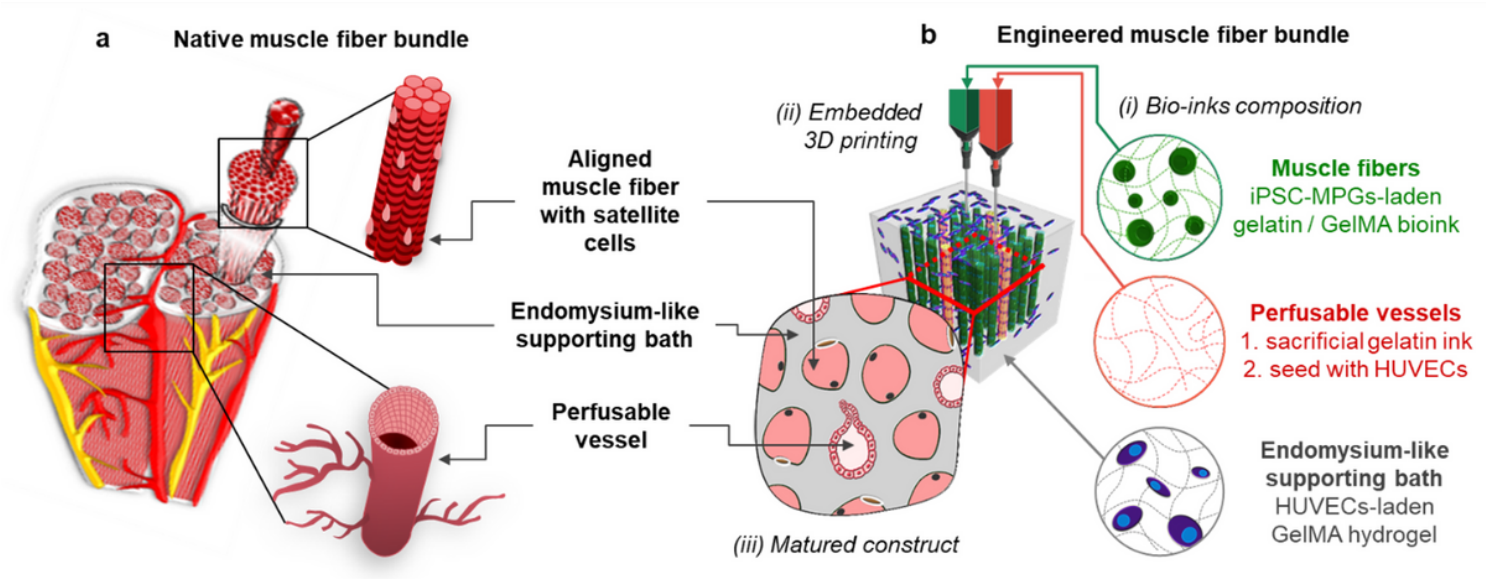

Figure 1

Schematic representation of bio-inspired engineering volumetric muscle tissue. (a) Native muscle tissue consists of muscle fiber bundles with a complex multiscale hierarchical architecture including muscle fibers and a vascular network embedded in endomysium (i.e., connective tissue). (b) We explored embedded multi-material bioprinting (EMB) to manufacture constructs that (partly) emulate this complex natural design, which is expected to enable the engineering of larger and more functional muscle tissues.

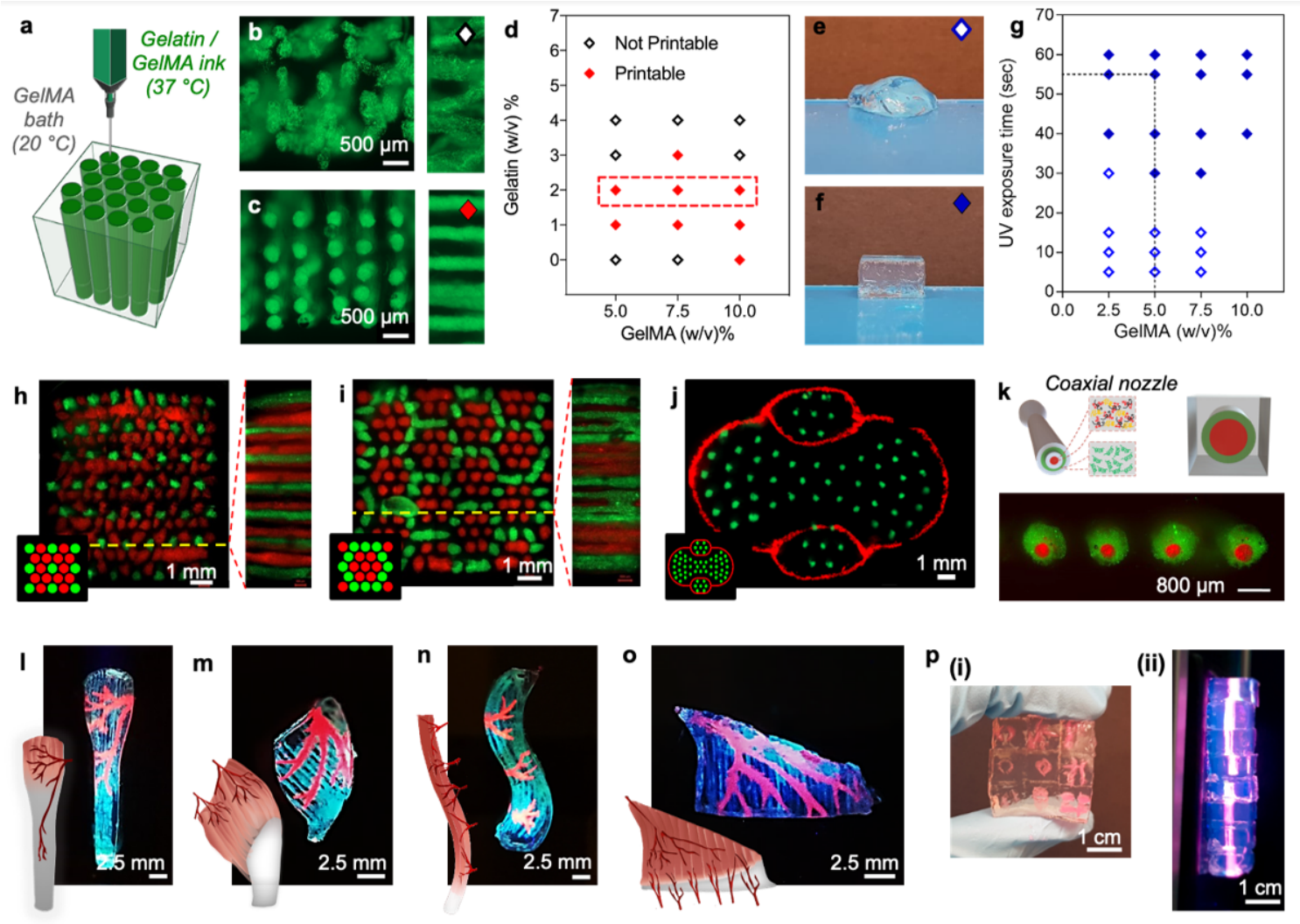

Figure 2

Embedded multi-material bioprinting of muscle architectures. (a) Temperature-controlled 3D printing for creating micropatterns of gelatin ink within a GelMA supporting matrix. (b) Printing 5% (w/v) GelMA bioink at 37 °C in a 5% (w/v) GelMA supporting bath at 20 °C resulted in poor printing fidelity characterized by a significant merging of the printed channels. (c) Printing 10% (w/v) GelMA at 37 °C in a 5% (w/v) GelMA supporting bath at 20 °C resulted in good printing fidelity. Increasing the GelMA concentration (10% w/v) resulted in more than ~80% of channels maintaining their structural integrity compared with printing of low concentration (5% w/v) of bioink which showed poor printing fidelity. (d) Analyzing different gelatin and GelMA concentrations revealed a printable working range. 2% (w/v) gelatin was used for further experimentation (dashed box). Using 5% (w/v) GelMA bioink with 1-2% (w/v) gelatin, we were able to successfully print shape-stable straight and non-merged parallel patterns. (e-g) We set out to use a photocrosslinking strategy to transform the embedding bath including the printed patterns into a solid hydrogel scaffold that was robust enough to enable in vitro culture, in vivo implantation, and eventually muscle tissue repair. To this end, various GelMA concentrations and photocrosslinking conditions (i.e., UV exposure time) were assessed to obtain a solid construct with mechanical properties optimized for muscle stem cell differentiation and maturation. 5% (w/v) GelMA

and a UV exposure time of 55 seconds was used for further experimentation (dashed line). UV exposure times below 30 seconds (3 J/cm2) failed to completely solidify the embedding bath regardless of the GelMA concentration, but longer irradiation provided the required shape fidelity. (h-j) The optimized hydrogel formulations, printing parameters, and photocrosslinking method enabled the 3D printing of various well-aligned, micropatterned, multi-material 3D constructs, as visualized using fluorescence confocal microscopic cross sections (using inks spiked with red and green polystyrene nanoparticles). (k) Combining a coaxial nozzle with EMB enabled the fabrication of core-shell microfibers in the GelMA supporting matrix, which was confirmed by the cross-section view of fluorescence image. (l-o) Further combining the optimized 3D printing parameters with more advanced computer-aided designs readily enabled the printing of biomimetic engineered muscle tissue flaps. (p) Using GelMA ink as UV-glue enabled the assembly of 9 micropatterned blocks (~1 cm3) into a large complex construct.

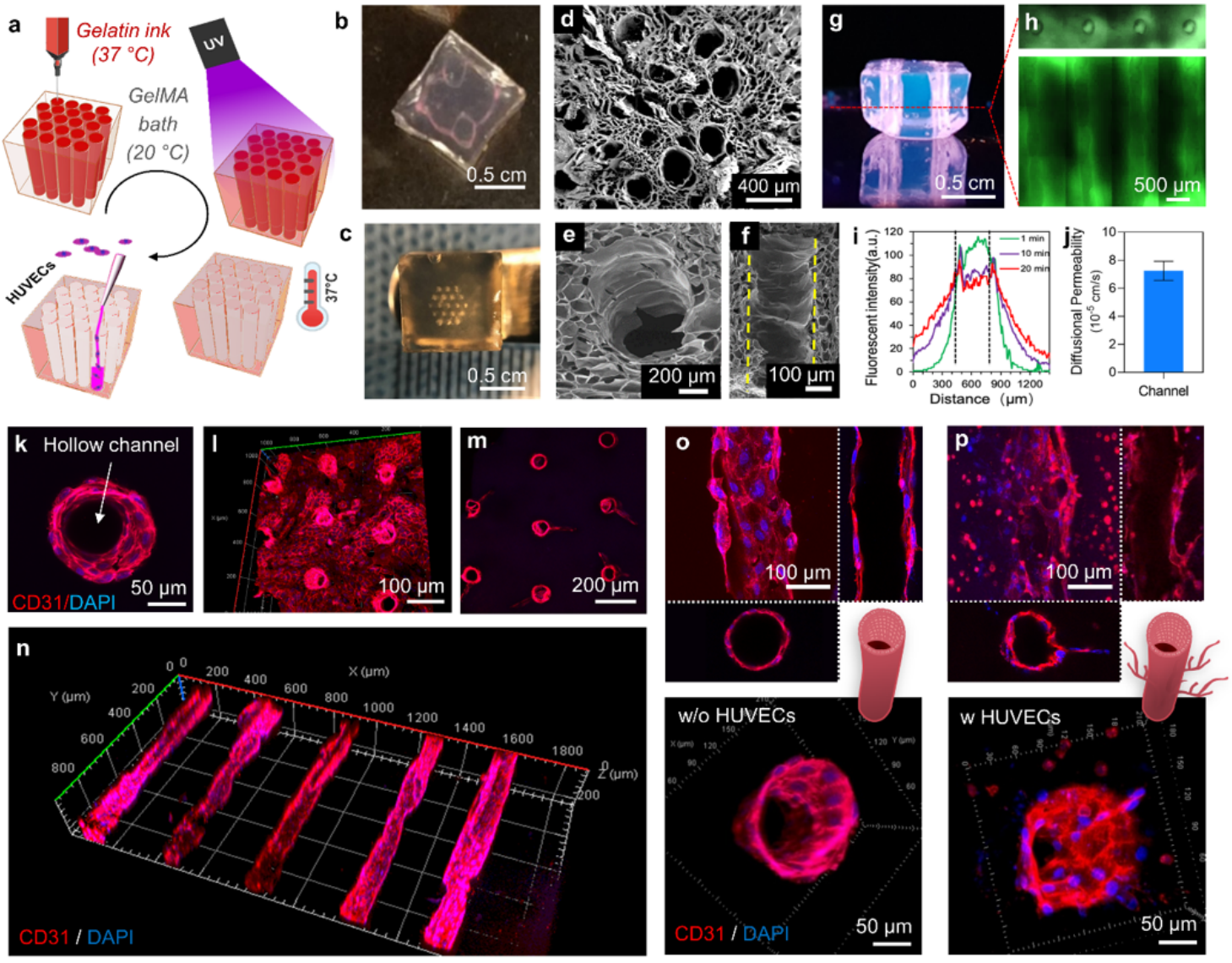

Figure 3

Vascularized construct engineering. (a) Schematic diagram showing the fabrication process of the endothelialized hollow perfusable channels using embedded printing. (b,c) Macrophotograph of a

photocrosslinked GelMA block with 3D printed gelatin bifurcating network (b) and parallel channels (c). The gelatin patterns could be dissolved by incubation at 37 °C, thereby forming hollow channels, as revealed by (d,e) transversal and longitudinal (f) cross sectional scanning electron microscopy imaging. (g,h) Channels were perfusable as shown by injection with a fluorescein-labeled dextran solution, (i,j) and time-lapse confocal analysis demonstrated efficient diffusion of the fluorophores from the channels into the GelMA construct. (k-o) Seeding HUVECs into the perfusable channels resulted in the formation of fully endothelialized perfusable channels throughout the construct as confirmed by confocal fluorescence imaging of positive CD31 staining after three weeks of culture. (p) Also embedding HUVECs in the GelMA (i.e., in addition to seeding HUVECs in the channels) promoted sprouting from the endothelialized channels into the bulk material.

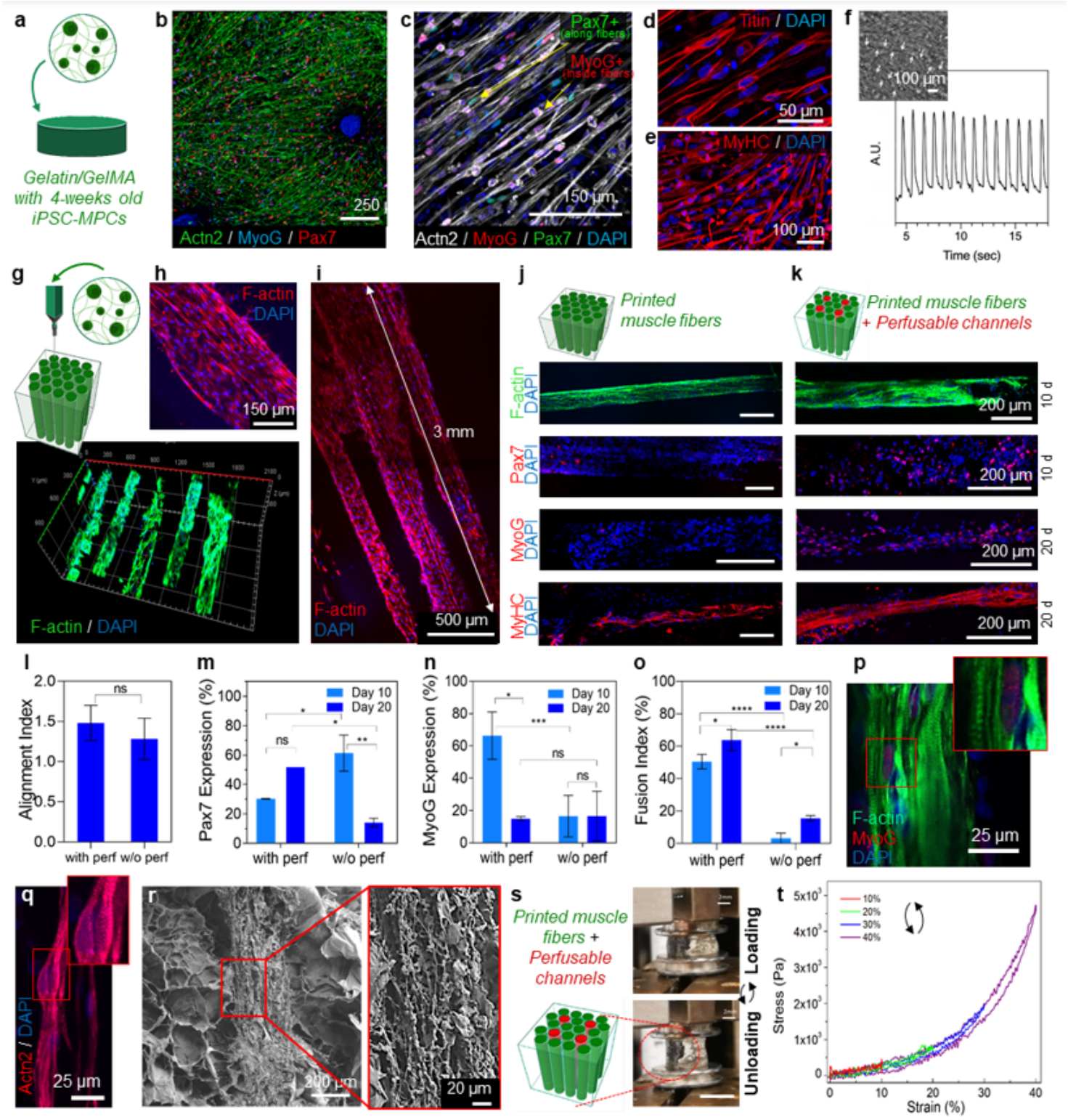

Figure 4

hiPSC-based muscle fiber bundle engineering. (a) hiPSC-MPCs were embedded in different gelatin/GelMA hydrogel formulations to identify the optimal conditions for cell survival, myogenic differentiation, and muscle repair. Gel mixtures containing 2% (w/v) gelatin, and 5%, 7.5%, or 10% (w/v) GelMA, that were shown to be printable inside a 5% (w/v) GelMA supporting matrix, were selected for this purpose 7.5% (w/v) GelMA / 2% (w/v) gelatin supported the long-term 3D in vitro culture and differentiation of hiPSC-

MPCs indicated by positive (b,c) Actn2, Pax7, MyoG, (d) Titin and (e) MyHC stainings. (f) Synchronized contraction (inset) of in situ formed fibrous structures (white arrows) corroborated the sustained function and muscle repair capacity of the 3D engineered tissue constructs. (g-i) The optimized hiPSC-MPCs laden hydrogel formulation also formed a bioink that could be printed within a photocrosslinkable GelMA support bath to engineer patterned (i.e., aligned) muscle fibers spanning the entire construct as confirmed by fluorescent confocal imaging of viable actin-stained cells. (j) After up to three weeks of in vitro culture, 3D printed muscle fibers were still viable and functional as confirmed by positive Actn2, Pax7, MyoG, and MyHC immunostaining. (k) Bioprinted hiPSC-laden constructs with perfusable vessels exhibited enhanced expression of myogenic stem cell and muscle maturation markers over the group without perfusion. The same muscle (stem) cell markers stained more prominently when the muscle fiber construct was endowed with perfusable vessels. (l) Alignment index of printed hiPSCs in constructs with and without perfusion was measured using fast Fourier transform analysis. Accordingly, both groups revealed highly aligned cellular fibers with no statistically significant difference ('ns': $p=0.667$; Mann-Whitney test; n=4). (m-o) The 3D printed constructs after 10 and 20 days of culture were immunostained against Pax7 (m), MyoG (n), and fusion index of matured muscle fibers expressing MyHC (o). Quantifying the expression percentage of these markers (i.e., % specific marker positive cells among the total number of DAPI-positive cells in a specific region of interest) revealed significant differences between the non-perfusable versus perfusable constructs ('*': $p<0.01$; '**': $p<0.0019$; '***': $p<0.0004$; '****': $p<0.0001$; Tukey's multiple comparisons test; n=3) (p,q) MyoG- and Actn2-positive cellular fibers with characteristic sarcomeric patterns where observed in the matured constructs. (r) Scanning electron microscopy showed aligned nanofibrous structures that where uniquely present in the printed gelatin/GelMA Channels, but not in the supporting GelMA bulk material. (s,t) Consecutive cyclic loading up to 40% strain showed no observable changes in stress-strain curves, indicating the compatibility of the 3D printed constructs with applications in continuously deforming tissues such as muscles.

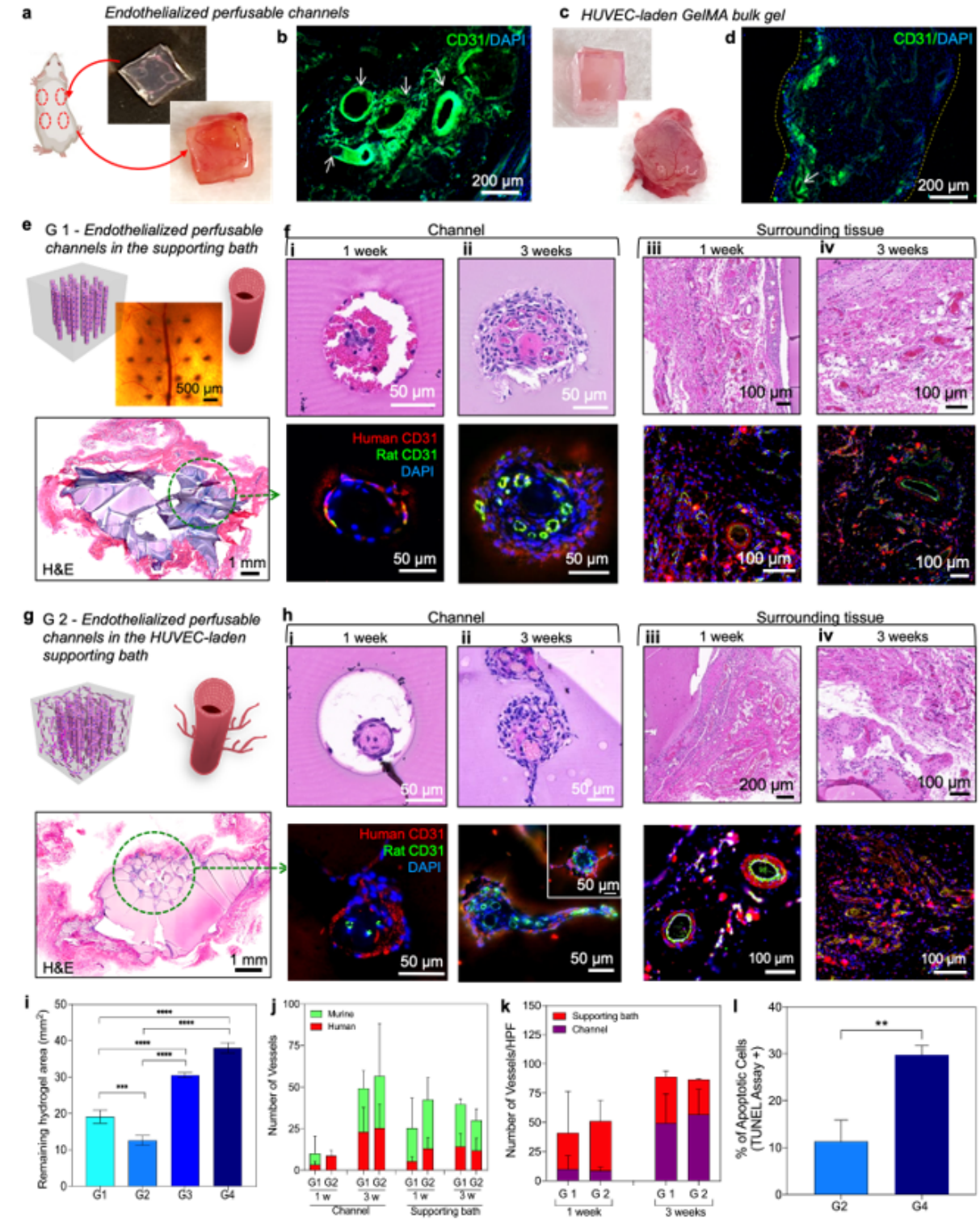

Figure 5

Prevascularized engineered muscle tissue integrated with the host. (a) Subcutaneous implantation of a bioprinted construct with bifurcating channel network in nude rats. (b) Immunostaining of the explanted construct stained with murine-positive CD31 (green) and DAPI (blue). The bioprinted vasculatures were invaded by the host's vasculature as indicated by the accumulation of murine-positive vasculature in the harvested sample. (c) Explanted bulk GelMA hydrogel followed by (d) immunostaining with murine-

positive CD31 and DAPI. H&E stained and immunostained images of G1 (e-f) and G2 (g-h) harvested on week 1 and week 3. Human-specific CD31 is colored in red and rat-specific CD31 is colored in green. Human-specific CD31 is colored in red and rat-specific CD31 is colored in green. (i) Remaining hydrogel area after harvesting the implanted samples on week 1. ('**': $p<0.0027$; '***': $p<0.0002$; '****': $p<0.0001$; Tukey's multiple comparisons test; n=5). (j) Number of vessels found in the murine-positive and human-positive CD31 immunostained samples after harvest on week 1 and week 3. ('ns': $p=0.8$; Sidak's multiple comparisons test; n=3). In the surrounding tissue, murine vessels were initially found more prevalently than human vessels. However, as the HUVECs grew out into the host tissue, the ratio of murine to human vessels decreased over time. (k) Number of total human and murine vessels per high-power field (HPF) found in the supporting bath and inside the channels after 1 and 3 weeks of in vivo culture ('ns': $p=0.57$; Sidak's multiple comparisons test; n=3). The formation of human and murine vessels could have been triggered much faster in presence of the ECs in the G2 supporting matrix. (l) Comparing the percentage of apoptotic cells in groups G2 and G4 using the results of TUNEL staining ('**': $p<0.0062$; unpaired t-test, n=4).

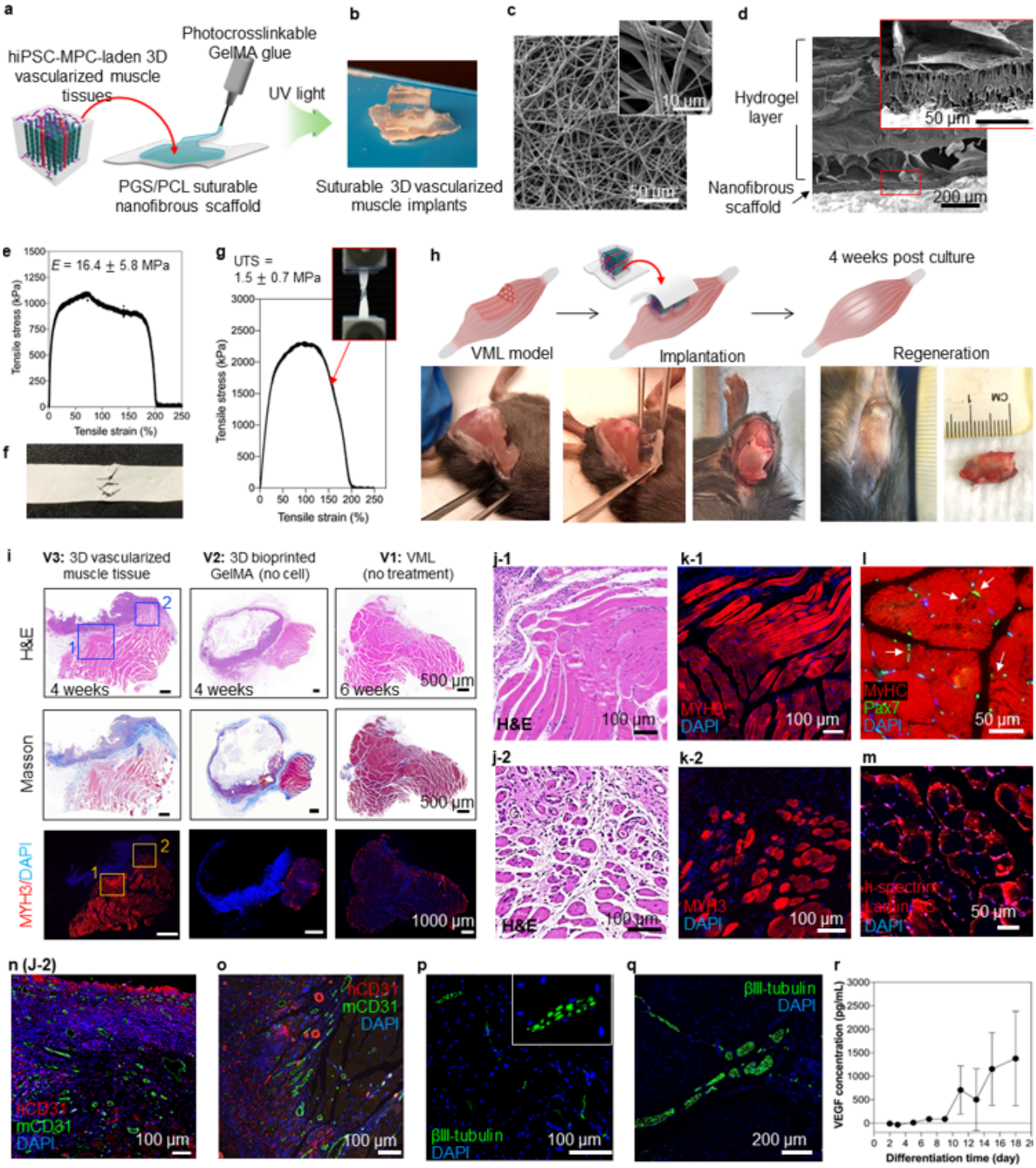

Figure 6

Evaluation of the regenerative potential of suturable 3D vascularized muscle implants using a VML model. (a) Schematic diagram of the composite construct preparation using a photocrosslinkable GelMA glue. (b) Obtained suturable 3D vascularized muscle implants. (c) Nanofibrous morphology of the PGS/PCL graft. (d) The interface between the GelMA supporting bath and the PGS/PCL graft that were strongly attached to each other. (e) Tensile stress-strain curve of the PGS/PCL graft. (f) Two pieces of the

PGS/PCL graft sutured together (n=3 for the number of samples tested). (g) Tensile stress-strain curve of the two sutured PGS/PCL grafts (n=3). (h) The suturable 3D vascularized muscle implants can be directly sutured into the VML injury site. Harvested quadriceps after 4 weeks implantation of the PGS/PCL graft showed that printed constructs integrated into the VML injury site. (i) H&E staining, Masson tri-chrome, and MYH3/DAPI staining images of the suturable 3D vascularized muscle implants with aligned hiPSC-MPCs and endothelialized perfusable channels, bulk GelMA hydrogel, and untreated VML after 4 weeks implantation. (j) H&E images at longitudinal (J-1) and a cross-sectional views (J-2) of the suturable 3D vascularized muscle implants (i). (k) Myosin heavy chain-embryonic (MYH3, red) and DAPI (blue) immunostaining images with longitudinal (k-1) and a cross-sectional view (k-2) of the suturable 3D vascularized muscle implants (i) to evaluate muscle development. (l) MyHC (red)/Pax7 (green)/DAPI (blue) and (m) human spectrin (red)/human lamin A/C (green)/DAPI (blue) immunostaining images of the suturable 3D vascularized muscle implants. (n,o) Human CD31 (red)/mouse CD31 (green)/DAPI immunostaining images of harvest samples near the implanted samples. (p,q) βIII-tubulin (green) and DAPI (blue) immunostaining images of harvested samples that were located near (p) newly generated muscle and (q) near the implanted samples. (r) Secreted VEGF from the 3D printed muscle tissue with aligned hiPSC-MPCs microfibers (n=3).

Supplementary Files

This is a list of supplementary files associated with this preprint. Click to download.

- Moviessupplementary.zip
- SupplementaryInformation.docx